Why Mean Potential Vorticity Cannot Be Materially Conserved in the Eddying Southern Ocean

GEOFFREY J. STANLEY[a,b] AND DAVID P. MARSHALL[b]

[a] *School of Mathematics and Statistics, University of New South Wales, Sydney, New South Wales, Australia*
[b] *Department of Physics, University of Oxford, Oxford, United Kingdom*

(Manuscript received 3 September 2021, in final form 25 February 2022)

ABSTRACT: Downstream of Drake Passage, the Antarctic Circumpolar Current (ACC) veers abruptly northward along the continental slope of South America. This spins down the ACC, akin to the western boundary currents of ocean gyres. During this northward excursion, the mean potential vorticity (PV) increases dramatically (decreases in magnitude) by up to a factor of 2 along mean geostrophic streamlines on middepth buoyancy surfaces. This increase is driven by drag near the continental slope, or by breaking eddies further offshore, and is balanced by a remarkably steady, eddy-driven decrease of mean PV along these northern circumpolar streamlines in the open ocean. We show how two related eddy processes that are fundamental to ACC dynamics—poleward buoyancy fluxes and downward fluxes of eastward momentum—are also concomitant with materially forcing PV to increase on the northern flank of a jet at middepth, and decrease on the southern flank. For eddies to drive the required mean PV decrease along northern streamlines, the ACC merges with the subtropical gyres to the north, so these streamlines inhabit the southern flanks of the combined ACC–gyre jets. We support these ideas by analyzing the time-mean PV and its budget along time-mean geostrophic streamlines in the Southern Ocean State Estimate. Our averaging formalism is Eulerian, to match the model's numerics. The thickness-weighted average is preferable, but its PV budget cannot be balanced using Eulerian 5-day averaged diagnostics, primarily because the z-level buoyancy and continuity equations' delicate balances are destroyed upon transformation into the buoyancy-coordinate thickness equation.

SIGNIFICANCE STATEMENT: The Antarctic Circumpolar Current is the world's largest ocean current and a key controller of Earth's climate. As the westerly winds that drive this current shift poleward under global warming, it is vital to know whether the current will follow. To begin addressing this, we study the current's fundamental dynamics, and constraints, under present-day conditions. By analyzing angular momentum and stratification together, we show that the current is weakened near boundaries and strengthened by eddies elsewhere. The strengthening effects of eddies are isolated to the current by merging the current with oceanic gyres to the north. This gives a new perspective on why the current travels so far northward alongside South America, and may provide dynamical constraints on future changes.

KEYWORDS: Southern Ocean; Eddies; Ocean dynamics; Potential vorticity

1. Introduction

The Antarctic Circumpolar Current (ACC) deflects steadily poleward while circumnavigating Antarctica, returning abruptly equatorward along the Argentine continental slope. This behavior is consistent with Ekman upwelling over the Southern Ocean north of Cape Horn, causing fluid columns to stretch and drift poleward, with an equatorward return flow confined to a narrow western boundary current. This is the paradigm of "Sverdrup balance" applied to an ocean gyre (Sverdrup 1947; Stommel 1957), or, in this case, to the Southern Hemisphere "supergyre" (Ridgway and Dunn 2007). Extending this paradigm to the ACC, including the latitudes of Drake Passage, is challenged by a lack of continental barriers, without which there can be no equatorward boundary current to balance the otherwise poleward flow induced by the wind stress curl at these latitudes.

One proposed extension is an "eddy Sverdrup balance," where Sverdrup balance is augmented by the eddy-induced downwelling, added alongside the Eulerian-mean upwelling that it largely negates. In an idealized reduced-gravity channel model, Marshall et al. (2016) witnessed such a three-way balance involving the Eulerian-mean northward velocity, the Eulerian-mean vertical velocity, and the eddy-induced vertical velocity. This result may be particular to the reduced-gravity formulation, but it cannot be correct in the real ACC: the eddy-induced velocity is only relevant in the context of fluxing tracers or momentum, arising as it does from correlations between the instantaneous velocity and tracers or momentum. In Sverdrup balance, no such eddy correlations arise: the planetary vorticity is time invariant, so its time-mean

---

Denotes content that is immediately available upon publication as open access.

Corresponding author: Geoffrey J. Stanley, g.stanley@unsw.edu.au

DOI: 10.1175/JPO-D-21-0195.1

advection is simply its advection by the time-mean velocity, not by any residual (time-mean plus eddy-induced) velocity.

Instead, in the Drake Passage latitudes, one must consider the more general form of Sverdrup balance, namely, the barotropic vorticity equation, wherein all torques are retained, not just the wind stress curl. Which additional torque is most important? It is well known that bottom form stress removes the vast majority of zonal momentum input by the westerly winds in the Drake Passage latitudes (Munk and Palmén 1951; Masich et al. 2015). Therefore, the analog of bottom form stress in the barotropic vorticity equation, namely, the bottom pressure torque, is of prime importance in these latitudes (Hughes and De Cuevas 2001; Lu and Stammer 2004). Indeed, the ACC extends to the seafloor and must navigate considerable topographic relief, inducing a vertical bottom velocity that may be an order of magnitude larger than the Ekman upwelling velocity, locally.

Moving from barotropic dynamics to layer-wise dynamics, it is also well known that eddy form stress (also called interfacial form stress) is largely responsible for transferring eastward momentum imparted by the surface winds downward to the seafloor, where it is removed by bottom form stress (Johnson and Bryden 1989). The same logic as above should apply: the curl of the eddy form stress divergence should be a dominant term, locally and in the net, in the layer-wise residual vorticity budget in the Drake Passage latitudes.

Now, dividing the residual vorticity budget by the mean layer thickness (the vertical separation between buoyancy surfaces) yields a residual potential vorticity (PV) equation. It stands to reason that a dominant term in the residual PV budget is the curl of the eddy form stress divergence divided by the mean layer thickness. With such a dominant forcing term present in the Drake Passage latitudes, we should not expect the mean PV to be materially conserved, following the residual velocity, in the eddying Southern Ocean. Rather, varying mean PV along streamlines of the ACC is part-and-parcel of how the ocean navigates these circumpolar latitudes.

The variation of PV along streamlines in the ACC has been studied, most notably by Gille (1997). Our results agree with Gille's key result, that mean PV rises dramatically along streamlines transiting Drake Passage and the Argentine slope, balanced by PV decreasing along streamlines elsewhere. However, different model data and numerical methods alter the finer details and interpretation. In particular, Gille attributes PV decreasing along streamlines to large-scale patterns in Ekman upwelling. However, subsequent advances in understanding the residual overturning circulation of the Southern Ocean (Danabasoglu et al. 1994; Gent et al. 1995; Marshall 1997; Marshall and Radko 2003) indicate that eddy-induced downwelling largely compensates the Ekman upwelling of the Eulerian-mean Deacon cell. Instead, we argue that eddies are the agents of such PV forcing along deep ACC streamlines, and this eddy PV forcing is concomitant with downward eddy form stress and poleward eddy buoyancy fluxes. In summary, this paper attempts to update Gille's (1997) important findings in light of theoretical and modeling development over the past two decades.

A word on averaging formalisms is in order, since eddy forcings are defined by the choice of averaging operator. From a theoretical perspective, the thickness-weighted average (TWA) formalism (Young 2012) has emerged as the ideal averaging technique, since it effectively captures the residual overturning of the Southern Ocean. Under TWA, averages are taken following buoyancy surfaces as they heave vertically, and are weighted by the layer thickness to account for the bolus transport. Unfortunately, we found the TWA PV budget using 5-day Eulerian-averaged outputs from a z-level model cannot be closed. The primary numerical issue, detailed in appendix C, is that the buoyancy and continuity equations are extremely delicate, and do not survive the transformation off their native z-level grids. Nonetheless, the mean PV, whether from TWA or Eulerian averages, exhibits the same qualitative structure along ACC streamlines (appendix B). Hence, we employ Eulerian averaging, which enables closure of the PV budget in a z-level ocean model.

Section 2 pedagogically describes why PV cannot be conserved in the eddying Southern Ocean, using large-scale approximations. These approximations are removed in section 3, which describes the Ertel PV appropriate for a numerical ocean model, with numerical methods detailed in appendix A. The structure and forcing of PV along geostrophic streamlines in the ACC are studied in sections 4 and 5, before concluding in section 6.

2. From vorticity to potential vorticity

Eddies play a key role in ocean dynamics through eddy form stress, eddy buoyancy fluxes, eddy-induced velocity, and PV diffusion. Since all of these are different manifestations of the same physical process, there is great scope for double-counting the effects of eddies. This confusion is evidenced by the discussion in Warren et al. (1996); see subsequent replies by Hughes (1997) and Olbers (1998). As such, the averaged equations should be derived carefully and systematically. This section provides a pedagogical derivation, deriving the linear vorticity budget, with or without some common approximations, then linking this to the large-scale PV budget.

a. Notation and setup

For simplicity (of presentation only), we use a Cartesian coordinate system with eastward, northward, and upward coordinates (x, y, z) and orthonormal basis vectors $(\hat{\mathbf{i}}, \hat{\mathbf{j}}, \hat{\mathbf{k}})$, and t the time coordinate. Let an overbar denote the arithmetic time-mean—which when applied a function of Cartesian coordinates (x, y, z, t) gives the Eulerian time-mean. Let p be the pressure, ρ the in situ density, $\rho_0(z)$ a reference density profile, ρ_c the Boussinesq reference density, g the (constant) gravitational acceleration, $\mathbf{u} = u\hat{\mathbf{i}} + v\hat{\mathbf{j}}$ the horizontal velocity, and $\mathbf{v} = \mathbf{u} + w\hat{\mathbf{k}}$ the 3D velocity. The (spatial) gradient of a scalar field a is $\nabla a \equiv a_x\hat{\mathbf{i}} + a_y\hat{\mathbf{j}} + a_z\hat{\mathbf{k}}$. The 2D gradient of a at constant height is denoted $\nabla_z a = a_x\hat{\mathbf{i}} + a_y\hat{\mathbf{j}}$. The vertical component of a vector's curl is denoted $\nabla_z \times (a\hat{\mathbf{i}} + b\hat{\mathbf{j}} + c\hat{\mathbf{k}}) = b_x - a_y$.

b. *Vorticity balance*

Multiplying the continuity equation $\nabla \cdot \mathbf{v} = 0$ by the Coriolis parameter f and applying the product rule yields one form of the vorticity balance,

$$\beta v = f w_z + \nabla \cdot (f\mathbf{u}), \tag{1}$$

where $\beta = f_y$ and $f_z = 0$. Only the ageostrophic flow contributes to $\nabla \cdot (f\mathbf{u})$, but we temporarily leave this expressed with the full flow. No eddy terms arise when time-averaging (1), hence

$$\beta \overline{v} = f \overline{w}_z + \nabla \cdot (f \overline{\mathbf{u}}). \tag{2}$$

The same treatment applied to a nondivergent eddy-induced velocity $\mathbf{v}^*$ yields the eddy vorticity balance,

$$\beta v^* = f w_z^* + \nabla \cdot (f\mathbf{u}^*). \tag{3}$$

Adding (2) and (3) gives the residual (mean plus eddy) vorticity balance,

$$\beta(\overline{v} + v^*) = f(\overline{w} + w^*)_z + \nabla \cdot (f\overline{\mathbf{u}} + f\mathbf{u}^*). \tag{4}$$

This equation, postulated as relevant to the ACC, is merely two balances combined as one. The mean flow must satisfy its own vorticity balance (2) independently of that for the eddying flow (3), and vice versa.

Whereas both the mean and eddy-induced velocities pierce mean buoyancy surfaces, the residual velocity is closely aligned with these surfaces; this will help to frame the PV equation. But first, the above vorticity budgets are cast in a more familiar form.

c. *Approximate vorticity balance*

The horizontal momentum equation is approximately

$$\rho_c \hat{\mathbf{k}} \times f\mathbf{u} = -\nabla_z p + \boldsymbol{\tau}_z, \tag{5}$$

where $\boldsymbol{\tau}$ is the vertical stress. Neglected terms (lateral viscous stresses, tendency, and nonlinear terms) can be carried alongside $\boldsymbol{\tau}_z$ if desired. The geostrophic velocity $\mathbf{u}_g = (\rho_c f)^{-1}\hat{\mathbf{k}} \times \nabla_z p$ satisfies $\nabla \cdot (f\mathbf{u}_g) = 0$. The ageostrophic velocity $\mathbf{u}_{\text{ag}} = \mathbf{u} - \mathbf{u}_g$ satisfies $\nabla \cdot (f\mathbf{u}_{\text{ag}}) = \rho_c^{-1}\nabla_z \times \boldsymbol{\tau}_z$. Thus, (5) turns (1) into the approximate vorticity balance, the time-mean version of which is

$$\beta \overline{v} = f\overline{w}_z + \rho_c^{-1}\nabla_z \times \overline{\boldsymbol{\tau}}_z. \tag{6}$$

Considering eddies, the Gent et al. (1995) parameterization defines the horizontal eddy-induced velocity as

$$\mathbf{u}^* = -\frac{\partial}{\partial z}\left(\frac{\overline{\mathbf{u}'b'}}{N^2}\right), \tag{7}$$

where the buoyancy b (see section 3a) is assumed to be quasi-materially conserved, $N^2 = \overline{b}_z$ is the mean stratification, and b' and $\mathbf{u}'$ are fluctuations from their Eulerian time-means $\overline{b}$ and $\overline{\mathbf{u}}$. Making the standard assumptions that (i) fluctuations in the height of a buoyancy surface, ξ', are related to fluctuations in local buoyancy b' by $\xi' = -b'/N^2$, and (ii) fluctuations of the horizontal velocity $\mathbf{u}'$ are geostrophic so that $f\mathbf{u}' = \rho_c^{-1}\hat{\mathbf{k}} \times \nabla_z p'$, then (7) yields

$$f\mathbf{u}^* = -\rho_c^{-1}\hat{\mathbf{k}} \times \boldsymbol{\tau}_z^* \tag{8}$$

where

$$\boldsymbol{\tau}^* = -\overline{\xi'\nabla_z p'} \tag{9}$$

is the eddy form stress.[1] Thus, $\nabla \cdot (f\mathbf{u}^*) = \rho_c^{-1}\nabla_z \times \boldsymbol{\tau}_z^*$, transforming (3) into the approximate eddy vorticity balance,

$$\beta v^* = f w_z^* + \rho_c^{-1}\nabla_z \times \boldsymbol{\tau}_z^*. \tag{10}$$

d. *Approximate residual vorticity balance*

Adding (6) and (10) gives the approximate residual vorticity budget,

$$\beta(\overline{v} + v^*) = f(\overline{w} + w^*)_z + \rho_c^{-1}\nabla_z \times (\overline{\boldsymbol{\tau}} + \boldsymbol{\tau}^*)_z. \tag{11}$$

Under nonacceleration conditions, the residual overturning circulation vanishes, i.e., $\overline{v} + v^* = 0$ and $\overline{w} + w^* = 0$, which also implies $\nabla_z \times (\overline{\boldsymbol{\tau}} + \boldsymbol{\tau}^*)_z = 0$. However, nonacceleration conditions should only (approximately) hold under a zonal integral. In practice, the eddy field is patchy, and the local balance of (11) holds only because its two constituents, (6) and (10), hold locally as three-way balances.

The stretching terms (fw_z) will be annihilated when forming a PV equation, but the stress divergences will remain, translating into potentially significant PV forcings. Before moving to the PV budget, we first derive and discuss Sverdrup balance.

e. *Barotropic vorticity balance and Sverdrup balance*

Following Hughes and De Cuevas (2001), integrate (5) from the seafloor at $z = -H$ to the sea surface at $z = 0$ (assuming a rigid lid for simplicity of presentation), apply the Leibniz integral rule to the integrated pressure gradient, and finally cross differentiate to get the (approximate) barotropic vorticity balance,

$$\rho_c \beta V = \nabla_z \times [\boldsymbol{\tau}]_{-H}^{0} + \nabla_z \times (p_b \nabla H), \tag{12}$$

where $V = \int_{-H}^{0} v\,dz$ is the depth-integrated meridional flow, $p_b = p|_{z=-H}$ is the bottom pressure, and $[\boldsymbol{\tau}]_{-H}^{0} = \boldsymbol{\tau}|_{z=0} - \boldsymbol{\tau}|_{z=-H}$ is the vertical stress difference between the sea surface and seafloor. As before, no eddy terms arise when averaging (12).

Sverdrup balance is a special case of (12) (or its time-mean version) that retains only the planetary vorticity advection and the surface wind stress:

$$\beta V = \rho_c^{-1}\nabla_z \times \boldsymbol{\tau}|_{z=0}. \tag{13}$$

---

[1] A similar result can be obtained more carefully from the TRM-II theory of McDougall and McIntosh (2001). Also note the equivalence between $\boldsymbol{\tau}_z^*$ and the final term in the Eliassen–Palm divergence E^u in (C13): simply use $p_x = \phi_x = m_{\tilde{x}}$ from (C8e) and $\partial_z = h^{-1}\partial_{\tilde{b}}$ from (C1c) and (C2c).

The wind stress curl is generally negative in the Southern Ocean, inducing a southward Sverdrup flow. But the zonal integral of βV must be zero to maintain mass balance (ignoring evaporation, precipitation, and river runoff). Thus, other terms in (12) must be important—particularly the bottom pressure torque, $\nabla_z \times (p_b \nabla H)$. In the oceanic gyres, the Sverdrup flow is also generally single-signed, so the bottom pressure torque—which is nonlocally linked to the wind stress curl (Stewart et al. 2021)—establishes a western boundary current whose meridional mass flux balances that of the interior Sverdrup flow. The Drake Passage latitudes lack boundaries to support such a boundary current, so the bottom pressure torque becomes geographically distributed; it alternates in sign and locally swamps the wind stress curl, inducing a depth-integrated meridional flow with a complicated spatial structure, though zonally integrating to zero (Hughes and De Cuevas 2001). As the bottom pressure torque is linked to the topographic structure and largely balances the residual between the wind stress curl and the net meridional flow (i.e., the failure of Sverdrup balance), its rich structure is also seen in non-eddy-resolving models (Lu and Stammer 2004).

This patchy nature of the barotropic vorticity balance is concomitant with a similarly patchy nature of the vorticity balance on buoyancy surfaces. The eddy form stress $\boldsymbol{\tau}^*$ that transfers momentum down from the sea surface to the seafloor exhibits a similarly complicated spatial structure, typically enhanced downstream of major topographic obstacles (MacCready and Rhines 2001; Tansley and Marshall 2001). This eddy form stress, as we show next, appears in the PV budget, thereby inducing large and spatially complicated material changes in PV on interior buoyancy surfaces.

f. Large-scale potential vorticity budget

The preceding residual vorticity balance equations were intrinsically the sum of mean and eddy balances, because time-invariant quantities like f and β multiplied the velocity components. However, the large-scale PV, $f\overline{b}_z$, is time varying, so the residual equation for its material derivative cannot be similarly split.

This prompts introduction of the residual velocity, $\mathbf{v}^\dagger = \overline{\mathbf{v}} + \mathbf{v}^*$, which is nearly aligned with mean buoyancy surfaces. More precisely, the mean buoyancy is nearly materially conserved following the residual velocity, not the mean velocity:

$$\overline{b}_t + \overline{\mathbf{v}} \cdot \nabla \overline{b} = \overline{\boldsymbol{\varpi}} - \nabla \cdot (\overline{\mathbf{v}' b'}) \tag{14}$$

has large RHS, whereas

$$\overline{b}_t + \mathbf{v}^\dagger \cdot \nabla \overline{b} = \boldsymbol{\varpi}^\dagger \tag{15}$$

has a RHS $\boldsymbol{\varpi}^\dagger = \overline{\boldsymbol{\varpi}} + \nabla \cdot (\mathbf{v}^* \overline{b} - \overline{\mathbf{v}' b'})$ much nearer zero.

To get the large-scale PV equation, multiply the residual vorticity balance (4) by $\overline{b}_z$:

$$\mathbf{v}^\dagger \cdot \nabla (f \overline{b}_z) - (f \mathbf{v}^\dagger \cdot \nabla \overline{b})_z + f \mathbf{v}_z^\dagger \cdot \nabla \overline{b} = f w_z^\dagger \overline{b}_z + \overline{b}_z \nabla \cdot (f \mathbf{u}^\dagger). \tag{16}$$

The LHS was obtained by returning $\overline{b}_z \beta \mathbf{v}^\dagger$ to its advective form $\overline{b}_z \mathbf{v}^\dagger \cdot \nabla f$, then manipulating twice with the product rule. Crucially, the vortex stretching term $f \overline{b}_z w_z^\dagger$ on the RHS cancels with part of the last term on the LHS. Next, replace the buoyancy advection term using (15) to obtain

$$\begin{aligned} \mathbf{v}^\dagger \cdot \nabla (f \overline{b}_z) - (f \boldsymbol{\varpi}^\dagger - f \overline{b}_t)_z &= -f \mathbf{u}_z^\dagger \cdot \nabla \overline{b} + \overline{b}_z \nabla \cdot (f \mathbf{u}^\dagger) \\ &= \nabla \overline{b} \cdot \nabla \times (\widehat{\mathbf{k}} \times f \mathbf{u}^\dagger). \end{aligned} \tag{17}$$

So far, the only approximation is Boussinesq's. The LHS contains all ingredients for the material derivative of the large-scale PV. We now break the RHS into mean and eddy parts and apply approximations as in section 2c. Assuming hydrostatic balance, $\overline{p}_z = -g\overline{\rho}$, and (5), then

$$\nabla \overline{b} \cdot \nabla \times (\widehat{\mathbf{k}} \times f \overline{\mathbf{u}}) = g \rho_c^{-1} [\overline{\rho}_x \overline{b}_y - \overline{\rho}_y \overline{b}_x] + \rho_c^{-1} \nabla \overline{b} \cdot \nabla \times \overline{\boldsymbol{\tau}}_z. \tag{18}$$

Taking b as a function only of ρ and z annihilates the bracketed (solenoidal) term. The eddy part is simplified similarly, but using (8) to give

$$\nabla \overline{b} \cdot \nabla \times (\widehat{\mathbf{k}} \times f \mathbf{u}^*) = \rho_c^{-1} \nabla \overline{b} \cdot \nabla \times \boldsymbol{\tau}_z^*. \tag{19}$$

Putting (18) and (19) into (17) yields the residual large-scale PV balance:

$$(f \overline{b}_z)_t + \mathbf{v}^\dagger \cdot \nabla (f \overline{b}_z) = f \boldsymbol{\varpi}_z^\dagger + \frac{\nabla \overline{b} \cdot \nabla \times (\overline{\boldsymbol{\tau}} + \boldsymbol{\tau}^*)_z}{\rho_c}. \tag{20}$$

The LHS is the material derivative of the large-scale, mean PV following the residual velocity. The RHS provides its material forcings, namely, the tracer forcing gradient projected onto the large-scale vorticity, and the vorticity forcing projected onto the tracer gradient.

Following a similar procedure, the material derivative of large-scale mean PV following the Eulerian mean velocity is

$$(f \overline{b}_z)_t + \overline{\mathbf{v}} \cdot \nabla (f \overline{b}_z) = f \overline{\boldsymbol{\varpi}}_z + \frac{\nabla \overline{b} \cdot \nabla \times \overline{\boldsymbol{\tau}}_z}{\rho_c} - f (\overline{\mathbf{v}' \cdot \nabla b'})_z. \tag{21}$$

g. Discussion

Since the eddy form stress divergence is a large forcing of the residual momentum budget (and the eddy buoyancy flux divergence is a large forcing of the Eulerian-mean buoyancy budget), we can reasonably expect that the corresponding $\boldsymbol{\tau}^*$ (or $\overline{\mathbf{v}' \cdot \nabla b'}$) term will be a large forcing of the large-scale, mean PV in (20) [or (21)]. As such, the mean PV should not be expected to be conserved along mean ACC streamlines.

Mean streamlines in the ACC's northern extent, in particular, exhibit first-order variations of mean PV (Gille 1997, and our section 4). Moving downstream along these streamlines, PV rises markedly along the South American continental slope, balanced by a general decrease elsewhere. Gille (1997) suggested that wind forcing was primarily responsible for the latter effect, arguing that Ekman upwelling squeezes isopycnals toward the surface, thereby decreasing layer thickness and decreasing PV (toward larger negative values). However, the direct effect of wind on the mean PV, captured by the vertical stress divergence term in (20) or (21), is only significant in the upper few tens of meters. Beneath that, the wind stress only influences the PV budget indirectly, by impacting PV advection and eddy form stress, which are the dominant terms in the steady-state version of (20)—or for (21), by impacting PV advection and eddy buoyancy fluxes. We therefore argue that eddies, not winds, are the primary drivers of PV variations along ACC streamlines.

Beyond driving variations in general, can we also explain the sign of that eddy PV forcing, and is it consistent with the robust feature, mentioned above, that PV decreases moving downstream along northern ACC streamlines?

For simplicity, suppose the eddy form stress is zonal, $\boldsymbol{\tau}^* = \tau^*\hat{\mathbf{i}}$. In the ACC's core, $\tau^* > 0$, transporting eastward momentum downward, whereas $\tau^* \approx 0$ north and south of the ACC (where momentum input by the winds can be handled by leaning against topography—a type of bottom form stress). The vertical structure of τ^* has a subsurface maximum, increasing from near zero in the Ekman layer where viscous stress handles the downward momentum transport ($\overline{\boldsymbol{\tau}} \cdot \hat{\mathbf{i}} > 0$), to a subsurface maximum at a few hundred meters depth where the fastest growing baroclinic modes peak (Smith 2007), and back to zero below the level of topography where bottom form stress takes over. Thus, the northern flank of the middepth ACC should have $\tau^*_{yz} < 0$; taking $\nabla\overline{b} \approx \overline{b}_z\hat{\mathbf{k}}$, the eddy form stress forcing of PV in (20) is $-\rho_c^{-1}\overline{b}_z\tau^*_{yz} > 0$, materially increasing the PV. On the southern flank, eddy forcing should decrease PV.

A consistent conclusion is reached from the Eulerian perspective, wherein the northern flank of the ACC experiences Ekman convergence and a mean downwelling, largely compensated for by an eddy-induced upwelling. This eddy-induced upwelling advects high PV (low in magnitude) upward, increasing PV at the point in question. The reverse holds on the southern flank, with eddy-induced downwelling causing PV to decrease.[2]

The prediction is thus that eddy PV forcing increases PV moving downstream along northern ACC streamlines, away from boundaries. Yet, the opposite is observed: PV decreases. By investigating a numerical model, we shall see that the ACC adjusts its geography to avoid this apparent contradiction.

3. Ertel PV in a numerical ocean model

We use the Southern Ocean State Estimate (SOSE; Mazloff et al. 2010) spanning 2005–10 to diagnose the time-mean Ertel PV and its budget along time-mean geostrophic streamlines. The necessary theory is derived here, using the same approximations as made in SOSE: the Boussinesq approximation, hydrostatic balance, the traditional approximation, and its partner the thin-film approximation.

a. *Buoyancy and its surfaces*

Buoyancy is generally defined as $(-g/\rho_c)$ multiplied by a density variable that would ideally (i) be quasi-materially conserved, (ii) have isosurfaces that are everywhere tangent to the neutral tangent plane (McDougall 1987), and (iii) possess an exact geostrophic streamfunction on its isosurfaces (McDougall 1989; Stanley 2019b). Unfortunately, property (ii) is prevented by nonlinearities in the equation of state (McDougall and Jackett 1988).

Many density variables exist that approximate these properties, but only specific volume anomaly (Montgomery 1937) and orthobaric density (de Szoeke et al. 2000) satisfy property (iii), which is equivalent to annihilating the solenoidal term forcing an Ertel PV defined using that density variable (de Szoeke 2000)—essential for our purposes. We use specific volume anomaly, for computational simplicity and the ready availability of its partial derivatives. Future analyses might use (modified) topobaric surfaces (Stanley 2019a,b); however, these are 2D surfaces not 3D density fields, hindering the PV budget's calculation on the model's native z-level grid.

The in situ density ρ is determined by the equation of state R according to $\rho = R(S, \theta, p)$ where S is the salinity, θ the potential temperature, and p the pressure. Under the Boussinesq approximation, however, the equation of state takes a hydrostatic pressure determined from the height z: $\rho = R(S, \theta, -g\rho_c z)$ (Young 2010). This encourages using in situ density anomaly rather than specific volume anomaly (Stanley 2019b), hence we define buoyancy as

$$b(x, y, z, t) = -\frac{g}{\rho_c}[\rho(x, y, z, t) - R(S_0, \theta_0, -g\rho_c z)], \tag{22}$$

where S_0 and θ_0 are to-be-defined constants.

Let $\xi(x, y, b, t)$ denote height as a function of buoyancy in each water column, i.e., the inverse function of $b(x, y, z, t)$ for a given (x, y, t). Let $\xi^\#(x, y, b)$ denote height as a function of Eulerian time-mean buoyancy, i.e., the inverse function of $\overline{b}(x, y, z)$ for a given (x, y). The sharp notation, borrowed from the transformed residual mean (TRM; McDougall and McIntosh 2001) and TWA (Young 2012) theories, indicates a quantity constructed from mean fields, rather than a mean of some quantity. Indeed, $\xi^\#(x, y, b_0) \neq \overline{\xi(x, y, b_0, t)}$.

b. *Geostrophic streamfunction*

The exact geostrophic streamfunction for in situ density anomaly surfaces is the Montgomery (1937) potential, slightly modified for the Boussinesq approximation (Stanley 2019b),

$$\begin{aligned} m(x, y, z, t) = {} & \frac{1}{\rho_c} p_1(x, y, t) - \int_z^{z_1} b(x, y, z', t)dz' \\ & - b(x, y, z, t)z, \end{aligned} \tag{23}$$

where z_1 is a constant and $p_1(x, y, t) = p(x, y, z_1, t)$. To evaluate m on the chosen buoyancy surface, simply set $z = \xi(x, y, b_0, t)$, which also replaces $b(x, y, z, t)$ by the constant b_0.

---

[2] The major difference between (20) and (21) is that $\mathbf{v}^\dagger$ in (20) is nearly aligned with mean buoyancy surfaces, so the PV variation along mean buoyancy surfaces is clearly driven by the eddy form stress term. In contrast, $\overline{v}$ in (21) pierces mean buoyancy surfaces (e.g., mean Ekman downwelling), creating an advective PV forcing that is largely counterbalanced by the eddy buoyancy flux term. In the limit of vanishing $\overline{\varpi}$ and $\varpi^\dagger$, the residual between the mean PV advection and the eddy buoyancy flux PV forcing is the eddy-induced PV advection.

c. Instantaneous budgets

1) MOMENTUM BUDGET

The Boussinesq horizontal momentum equation in vector-invariant form, and the vertical momentum equation reduced to hydrostatic balance, are together written

$$\mathbf{u}_t + w\mathbf{u}_z + (f + \zeta)\hat{\mathbf{k}} \times \mathbf{u} + \nabla_z K + \nabla\phi = b_B\hat{\mathbf{k}} + \mathbf{F}, \tag{24}$$

where $\zeta = \upsilon_x - u_y$ is the relative vorticity's vertical component, $K = (u^2 + \upsilon^2)/2$ is the specific kinetic energy, $\phi = p\rho_c^{-1} + gz$ is the potential for the gravitational and pressure gradient accelerations, $b_B = -g\rho_c^{-1}(\rho - \rho_c)$ is the Boussinesq buoyancy [not to be confused with (22)], and $\mathbf{F} = F^{(X)}\hat{\mathbf{i}} + F^{(Y)}\hat{\mathbf{j}}$ captures the horizontal acceleration from viscosity, drag, and wind stress. Noting that $(\nabla \times \mathbf{u}) \times \mathbf{v} = \zeta\hat{\mathbf{k}} \times \mathbf{u} + w\mathbf{u}_z - K_z\hat{\mathbf{k}}$, and $f\hat{\mathbf{k}} \times \mathbf{u} = f\hat{\mathbf{k}} \times \mathbf{v}$, (24) becomes

$$\mathbf{u}_t + \boldsymbol{\omega} \times \mathbf{v} + \nabla B = b_B\hat{\mathbf{k}} + \mathbf{F}, \tag{25}$$

where $B = K + \phi$ is the Bernoulli potential, and

$$\boldsymbol{\omega} = f\hat{\mathbf{k}} + \nabla \times \mathbf{u} \tag{26}$$

is the absolute vorticity. The definition (26), rather than $2\Omega(\cos\varphi\hat{\mathbf{j}} + \sin\varphi\hat{\mathbf{k}}) + \nabla \times \mathbf{v}$, satisfies $\nabla \cdot \boldsymbol{\omega} = 0$ in the thin-film approximation (Dellar 2011).

2) BUOYANCY BUDGET

To obtain the material derivative of buoyancy, we require the material derivative of S, θ, and z (the latter trivial),

$$S_t + \mathbf{v} \cdot \nabla S = \dot{S}, \tag{27a}$$

$$\theta_t + \mathbf{v} \cdot \nabla\theta = \dot{\theta}, \tag{27b}$$

$$\mathbf{v} \cdot \nabla z = w, \tag{27c}$$

and the partial derivatives of b,

$$(\partial_S b)|_{\theta,z} = -\frac{g}{\rho_c}\frac{\partial R}{\partial S}(S, \theta, -g\rho_c z), \tag{28a}$$

$$(\partial_\theta b)|_{S,z} = -\frac{g}{\rho_c}\frac{\partial R}{\partial \theta}(S, \theta, -g\rho_c z), \tag{28b}$$

$$(\partial_z b)|_{S,\theta} = g^2\left[\frac{\partial R}{\partial p}(S, \theta, -g\rho_c z) - \frac{\partial R}{\partial p}(S_0, \theta_0, -g\rho_c z)\right]. \tag{28c}$$

We use ∂ notation to denote partial derivatives with respect to thermodynamic variables S, θ, and z; we use subscript notation to denote partial derivatives with respect to coordinate variables x, y, z, t. This helps distinguish the dual roles of z as a thermodynamic variable and a coordinate, which are related by $b_z = (\partial_S b)|_{\theta,z}S_z + (\partial_\theta b)|_{S,z}\theta_z + (\partial_z b)|_{S,\theta}$.

Now, $(\partial_S b)|_{\theta,z}$(27a) + $(\partial_\theta b)|_{S,z}$(27b) + $(\partial_z b)|_{S,\theta}$(27c) yields the buoyancy budget,

$$b_t + \mathbf{v} \cdot \nabla b = \boldsymbol{\varpi}, \tag{29}$$

where

$$b_t = (\partial_S b)|_{\theta,z}S_t + (\partial_\theta b)|_{S,z}\theta_t, \tag{30a}$$

$$\mathbf{v} \cdot \nabla b = (\partial_S b)|_{\theta,z}\,\mathbf{v} \cdot \nabla S + (\partial_\theta b)|_{S,z}\mathbf{v} \cdot \nabla\theta + (\partial_z b)|_{S,\theta}\mathbf{v} \cdot \nabla z, \tag{30b}$$

$$\boldsymbol{\varpi} = (\partial_S b)|_{\theta,z}\dot{S} + (\partial_\theta b)|_{S,z}\dot{\theta} + (\partial_z b)|_{S,\theta}w. \tag{30c}$$

The terms involving $(\partial_z b)|_{S,\theta}$ in (30b) and (30c) make relative contributions of less than 1%, so we ignore them henceforth.

3) ERTEL PV BUDGET

The instantaneous Boussinesq Ertel PV is

$$Q = \boldsymbol{\omega} \cdot \nabla b. \tag{31}$$

The material derivative of Q is derived via

$$\nabla b \cdot \nabla \times (25) + \boldsymbol{\omega} \cdot \nabla(29) \tag{32}$$

and uses $\nabla \cdot \boldsymbol{\omega} = 0$ and $\nabla \times \nabla b = 0$ to obtain the divergence of $(\mathbf{v} \cdot \nabla b)\boldsymbol{\omega} + (\boldsymbol{\omega} \times \mathbf{v}) \times \nabla b = (\boldsymbol{\omega} \cdot \nabla b)\mathbf{v} = Q\mathbf{v}$, then uses continuity,

$$\nabla \cdot \mathbf{v} = 0, \tag{33}$$

to obtain the PV advection. The result is

$$Q_t + \mathbf{v} \cdot \nabla Q = \nabla b \cdot \nabla \times \mathbf{F} + \boldsymbol{\omega} \cdot \nabla\boldsymbol{\varpi}. \tag{34}$$

The baroclinic production term $\nabla b \cdot (-g\rho_c^{-1}\nabla\rho) \times \hat{\mathbf{k}}$ vanishes because b is a function of ρ and z.

d. Time-mean: The Ertel–Euler PV

In a z-level model like SOSE, the natural averaging operator is the Eulerian time-mean. We define the "Ertel–Euler PV"—the Ertel PV formed from Eulerian averaged variables—as

$$Q^{\#} \equiv \overline{\boldsymbol{\omega}} \cdot \nabla\overline{b}. \tag{35}$$

The major advantage of $Q^{\#}$ is that its budget automatically closes upon closing the Eulerian time-mean momentum and buoyancy budgets. These are readily found by averaging (25) to get

$$\overline{\mathbf{u}_t} + \overline{\boldsymbol{\omega}} \times \overline{\mathbf{v}} + \overline{\boldsymbol{\omega}' \times \mathbf{v}'} + \nabla\overline{B} = \overline{b_B}\hat{\mathbf{k}} + \overline{\mathbf{F}} \tag{36}$$

and (29) to get

$$\overline{b_t} + \overline{\mathbf{v}} \cdot \nabla\overline{b} + \overline{\mathbf{v}' \cdot \nabla b'} = \overline{\boldsymbol{\varpi}}. \tag{37}$$

Proceeding as in the instantaneous case,

$$\nabla\overline{b} \cdot \nabla \times (36) + \overline{\boldsymbol{\omega}} \cdot \nabla(37), \tag{38}$$

yields the prognostic equation for $Q^{\#}$:

$$\begin{aligned} Q_t^{\#} + \overline{\mathbf{v}} \cdot \nabla Q^{\#} &= -\overline{\boldsymbol{\omega}} \cdot \nabla(\overline{\mathbf{v}' \cdot \nabla b'}) - \nabla\overline{b} \cdot \nabla \times (\overline{\boldsymbol{\omega}' \times \mathbf{v}'}) \\ &\quad + \nabla\overline{b} \cdot \nabla \times \overline{\mathbf{F}} + \overline{\boldsymbol{\omega}} \cdot \nabla\overline{\boldsymbol{\varpi}}, \end{aligned} \tag{39}$$

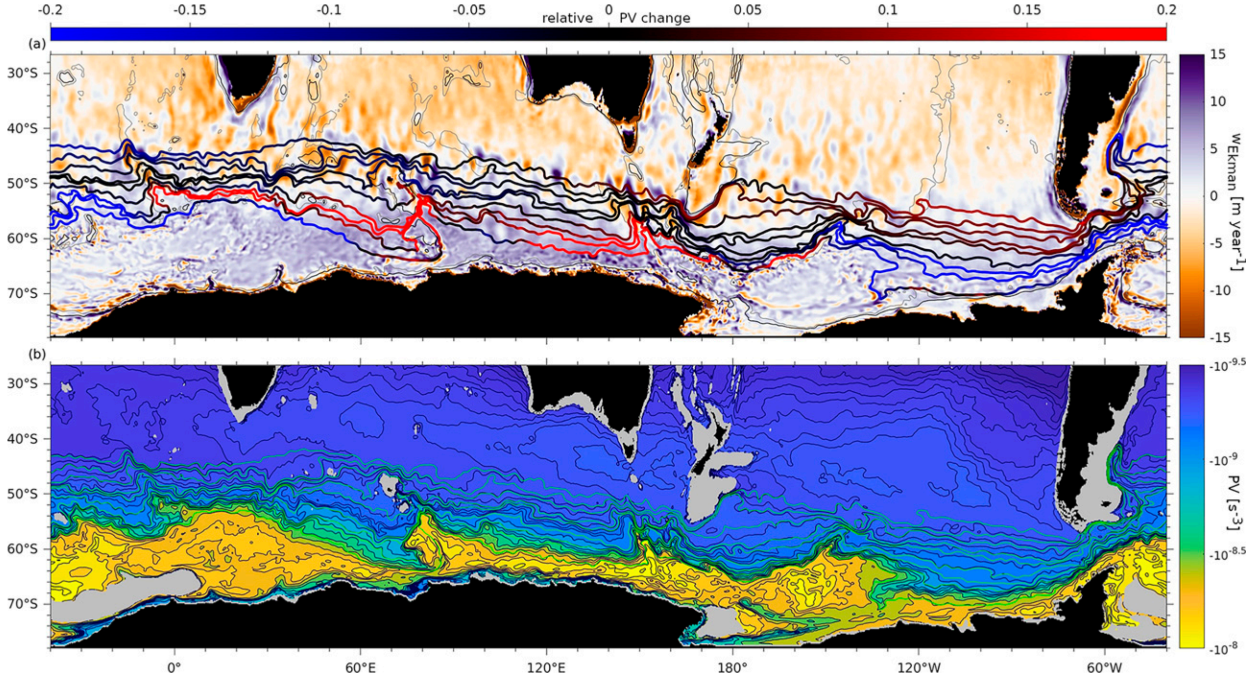

FIG. 1. (a) Mean vertical Ekman velocity (m yr^{-1}) and mean geostrophic streamlines (of $\overline{m}$) on the buoyancy surface $\overline{b} = b_0 = \overline{b}(133.25°\text{E}, 54.04°\text{S}, -700\ \text{m})$. Nine streamlines are shown, crossing 133.25°E at 50.5°, 52.0°, 53.4°, 54.9°, 56.4°, 58.0°, 59.5°, 61.0°, and 62.5°S (rounded). On streamlines, color (blue/black/red) indicates the relative change of the Ertel–Euler PV $Q^\#$ from its mean on each streamline; positive values indicate $Q^\#$ is less (more negative) than its mean. The 2000- and 3000-m isobaths, slightly smoothed, are contoured black and gray, respectively. (b) Ertel–Euler PV, $Q^\#$ (s^{-3}), on the same buoyancy surface as in (a), with contours at $-10^{-9-0.1n}$ and $-10^{-9+0.025n}$ for $n \in \mathbb{N}$ and the same nine streamlines (green). Gray regions indicate where the surface has incropped or outcropped.

where

$$Q^\#_t = \overline{\boldsymbol{\varpi}} \cdot \nabla \overline{b_t} + \overline{\boldsymbol{\varpi}}_t \cdot \nabla \overline{b}, \tag{40a}$$

$$\overline{\mathbf{v}} \cdot \nabla Q^\# = \overline{\boldsymbol{\varpi}} \cdot \nabla(\overline{\mathbf{v}} \cdot \nabla \overline{b}) + \nabla \overline{b} \cdot \nabla \times (\overline{\boldsymbol{\varpi}} \times \overline{\mathbf{v}}). \tag{40b}$$

From (39), the time-mean flow conserves the time-mean PV, except for eddy tracer effects, eddy vorticity effects, momentum forcing, and nonconservation of b.

The material derivative in (39) uses the Eulerian-mean velocity, but PV is best conserved following the residual velocity (section 2f). Ideally, we would employ the TRM-II theory of McDougall and McIntosh (2001), which is designed to approximate buoyancy-following averages using Eulerian averages. However, TRM-II requires the variance of a quasi-conservative density variable, which is lacking from SOSE's standard outputs—understandably so, since there is no universally best quasi-conservative density variable (section 3a). Computing this variance from SOSE's 5-day Eulerian averages may produce similar errors in TRM-II as arise when using TWA with SOSE's 5-day Eulerian averages (appendix C), so we have not pursued this further. Nonetheless, much can still be learned from the Ertel–Euler PV approach.

For the Eulerian-mean geostrophic function, no eddy terms arise and variables in (23) are simply replaced with their time-mean:

$$\overline{m}(x,y,z) = \frac{1}{\rho_c}\overline{p_1}(x,y) - \int_z^{z_1} \overline{b}(x,y,z')dz' - \overline{b}(x,y,z)z. \tag{41}$$

Our numerical methods are detailed in appendix A.

4. The structure of PV along streamlines

We now assess the structure of the Ertel–Euler PV along time-mean geostrophic streamlines in the ACC on the buoyancy surface defined by $\overline{b} = b_0$, where $b_0 = \overline{b}(x_0, y_0, z_0)$ with the reference location chosen as $x_0 = 133.25°\text{E}$, $y_0 = 54.0416°\text{S}$, and $z_0 = -700$ m, which further defines $S_0 = \overline{S}(x_0, y_0, z_0) = 34.44709$ and $\theta_0 = \overline{\theta}(x_0, y_0, z_0) = 2.834955°\text{C}$. For reference, this buoyancy surface roughly corresponds to a potential density (referenced to 0 dbar) surface of $\sigma_0 = 27.46$ kg m^{-3}, near the bottom of Antarctic Intermediate Water.

Figure 1 shows the geography of geostrophic streamlines on the $\overline{b} = b_0$ surface, as well as the vertical Ekman velocity and the relative change of $Q^\#$ along these streamlines (Fig. 1a) and $Q^\#$ itself (Fig. 1b). There are large $Q^\#$ variations along southerly streamlines where the surface shoals to near the base of the mixed layer, though $Q^\#$ is relatively well conserved through southern Drake Passage. In contrast, northern streamlines exhibit a dramatic rise in $Q^\#$ in the Drake Passage region, in agreement with Gille (1997), and a similar but

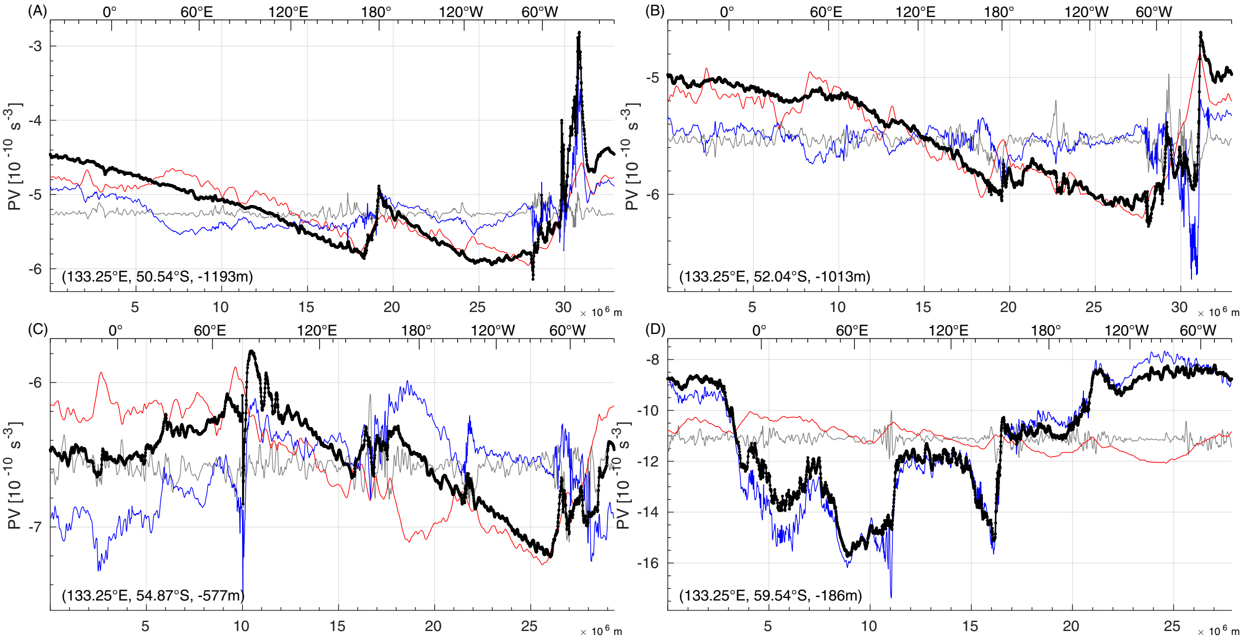

FIG. 2. The Ertel–Euler PV $Q^\#$ (thick black) along four streamlines A–D corresponding to the first, second, fourth, and seventh streamlines in Fig. 1 from north to south. The latitude and height at which they cross 133.25°E are indicated at the bottom left of each panel. Thin lines show the thin-film PV, $(f + \overline{v}_x - \overline{u}_y)\overline{b}_z$, when only the one of its three components is allowed to vary, with the other two terms set to their mean values along the streamline: Coriolis parameter f varies (red), stratification $\overline{b}_z$ varies (blue), and relative vorticity $\overline{v}_x - \overline{u}_y$ varies (gray). The abscissa is distance along the streamline, measured as the cumulative sum of the great circle distances between adjacent contour points. Top ticks indicate the first crossings every 10° of longitude.

smaller rise along Campbell Plateau; these are balanced by a steady decrease of $Q^\#$ elsewhere.

These $Q^\#$ variations are seen more clearly in Fig. 2, which shows $Q^\#$ (in black) along four streamlines: A, the northernmost circumpolar streamline; B, another northerly streamline, passing slightly further off the Argentine slope; C, the most southerly streamline that passes north of Kerguelen Plateau; and D, a southerly streamline passing between Kerguelen Plateau and Heard Island. Along streamline A, $Q^\#$ rises by ~50% through Drake Passage (~60°W), rises by ~15% along Campbell Plateau (~170°E), and drops steadily everywhere else. The steady rate of PV decrease is remarkable, given the richly heterogeneous eddy field of PV forcings. Along streamline C, $Q^\#$ decreases between Kerguelen Plateau (~70°E) and Drake Passage, and actually increases slightly on the approach to Kerguelen to pass north of the plateau. The structure of $Q^\#$ along streamline B is a mixture of that along streamlines A and C, with $Q^\#$ roughly constant between Drake Passage and Kerguelen Plateau. The largest fluctuations of $Q^\#$ along streamline D occur upstream and in the vicinity of Kerguelen Plateau. None of these streamlines exhibit the PV structure found by Gille (1997), who shows that PV is essentially constant in the Atlantic and Indian sectors, and that all PV decreases occur between Campbell Plateau and Drake Passage (her Fig. 7a). This is likely due to differences between SOSE and the Semtner–Chervin model that Gille (1997) analyzed (appendix B).

Figure 2 also shows how the thin-film PV approximation, $(f + \overline{\zeta})\overline{b}_z$, changes along streamlines A–D due to changes in its three components: f, $\overline{\zeta}$, and $\overline{b}_z$. Variations of $\overline{\zeta}$ are significant only at scales smaller than ~5° of longitude, in agreement with Gille (1997). Along streamline A, the PV decrease after Drake Passage and before Kerguelen is achieved by increasing $\overline{b}_z$, while the f contribution is fairly stable—as expected to remain north of Kerguelen. Downstream of Kerguelen on streamline A, PV decreases are mostly achieved by decreasing f as streamlines slowly migrate southward to meet Drake Passage, whereas $\overline{b}_z$ is relatively constant (except around Campbell Plateau). Along streamline B, PV decreases are achieved mostly by f variations as the streamline wends southward toward Drake Passage, while $\overline{b}_z$ variations are dominant only around Drake Passage, elsewhere just counterbalancing f variations on short scales. Streamline C shows large compensation between $\overline{b}_z$ and f variations, while streamline D remains consistently far south and is dominated by $\overline{b}_z$ variations.

Gille (1997) proposed a mechanism wherein Ekman upwelling squeezes isopycnals toward the surface, thereby increasing $|Q^\#|$ and decreasing $Q^\#$. However, Figs. 1a and 2a provide evidence against this hypothesis, as the fastest drop of $Q^\#$ on streamline A due to stratification changes occurs between ~10° and ~45°E, which is generally a region of Ekman downwelling, not upwelling. We shall discuss this further in the next section, after establishing a framework for the material forcing of $Q^\#$ along streamlines.

5. The forcing of Ertel–Euler PV along streamlines

a. Theory

A time-mean geostrophic streamline is a contour of constant $\overline{m}_0$, with line element $d\mathbf{s} = (\overline{\mathbf{u}_g}/|\overline{\mathbf{u}_g}|)ds$, where $\overline{\mathbf{u}_g} = (\rho_c f)^{-1}\hat{\mathbf{k}} \times \nabla\overline{m}_0$ is the time-mean geostrophic velocity. The change in $Q^{\#}$ over a distance s along such a streamline is

$$Q^{\#}(s) - Q^{\#}(0) = \int_0^s \nabla Q^{\#} \cdot d\mathbf{s} = \int_0^s \overline{\mathbf{u}_g} \cdot \nabla_b Q^{\#} \frac{ds}{|\overline{\mathbf{u}_g}|}, \qquad (42)$$

where ∇_b is the lateral gradient operator acting within the time-mean buoyancy surface.

To integrate the PV budget along streamlines, we first decompose the mean advection of PV into geostrophic and ageostrophic advection in the buoyancy surface, and vertical advection across the buoyancy surface, using the standard transformation $\nabla_b\Phi = \nabla_z\Phi + \Phi_z\nabla_b z$. This yields

$$\overline{\mathbf{v}} \cdot \nabla Q^{\#} = \overline{\mathbf{u}_g} \cdot \nabla_b Q^{\#} + \overline{\mathbf{u}_{\mathrm{ag}}} \cdot \nabla_b Q^{\#} + w^{\#} Q^{\#}_z, \qquad (43)$$

where the mean ageostrophic horizontal velocity is $\overline{\mathbf{u}_{\mathrm{ag}}} = \overline{\mathbf{u}} - \overline{\mathbf{u}_g}$, and

$$w^{\#} = \overline{w} - \overline{\mathbf{u}} \cdot \nabla_b \xi^{\#} \qquad (44)$$

is the mean vertical velocity minus that required by mean horizontal flow to stay on the mean buoyancy surface. The geostrophic advection of PV in (42) is replaced using (43), (39), and (40a) with $\overline{\boldsymbol{\omega}}_t = (f\hat{\mathbf{k}} + \nabla \times \overline{\mathbf{u}})_t = \nabla \times \overline{\mathbf{u}}_t$ to yield the streamwise PV budget:

$$\begin{aligned} Q^{\#}(s) - Q^{\#}(0) = \int_0^s (-\overline{\mathbf{u}_{\mathrm{ag}}} \cdot \nabla_b Q^{\#} \quad & - w^{\#} Q^{\#}_z \\ - \overline{\boldsymbol{\omega}} \cdot \nabla \overline{b}_t \quad & - \nabla\overline{b} \cdot \nabla \times \overline{\mathbf{u}}_t \\ - \overline{\boldsymbol{\omega}} \cdot \nabla \overline{\mathbf{v}' \cdot \nabla b'} \quad & - \nabla\overline{b} \cdot \nabla \times \overline{\boldsymbol{\omega}' \times \mathbf{v}'} \\ + \overline{\boldsymbol{\omega}} \cdot \nabla \overline{\boldsymbol{\varpi}} \quad & + \nabla\overline{b} \cdot \nabla \times \overline{\mathbf{F}}) \frac{ds}{|\overline{\mathbf{u}_g}|}. \end{aligned} \qquad (45)$$

b. Numerics

Computing the RHS of (42) and (45) requires care (the LHS was described in section 3). Regarding the integrated geostrophic advection of PV, the RHS of (42), the mean geostrophic velocity is staggered, with its zonal and meridional components living on the v grid (south edge) and u grid (west edge), respectively. This directly enables computing $\overline{\mathbf{u}_g} \cdot \nabla_b Q^{\#}$ using a centered second-order advection scheme with a five point stencil of $Q^{\#}$ on the surface. Then, the PV forcing $G = \overline{\mathbf{u}_g} \cdot \nabla_b Q^{\#}$ is bilinearly interpolated from the ζ grid to the streamline's contour points, then integrated as follows. The geostrophic speed $|\overline{\mathbf{u}_g}| = (\overline{u_g}^2 + \overline{v_g}^2)^{1/2}$ on the streamline is constructed by bilinearly interpolating each of $\overline{u_g}^2$ and $\overline{v_g}^2$ onto the streamline's contour points from the v grid and u grid, respectively. The distance, ds, is computed as the great circle distance between consecutive points on the streamline. Finally, $\int_0^s G|\overline{\mathbf{u}_g}|^{-1}\, ds$ is integrated trapezoidally along the streamline.

The result, however, cannot exactly match the LHS of (42), the true PV. To see why, consider a streamline passing south and east of the stencil's central point: the north and west $Q^{\#}$ values never enter the interpolation for $Q^{\#}(s)$ (the LHS), but they do affect $\overline{\mathbf{u}_g} \cdot \nabla_b Q^{\#}$ at the central point, and hence the reconstructed PV (the RHS). Nonetheless, these advection errors caused by numerical discretization will be acceptably small (see gray versus black curves in Fig. 3).

For the RHS of (45), most PV forcing terms G live natively on the same grid as $Q^{\#}$, so are handled exactly as above. The two exceptions are the ageostrophic and $w^{\#}$ advections, discussed next.

The zonal ageostrophic velocity $\overline{u_{\mathrm{ag}}} = \overline{u} - \overline{u_g}$ on the surface requires $\overline{u}$ on the surface v grid, obtained by averaging u onto the T grid, then linearly interpolating vertically onto the surface, then averaging horizontally onto the v grid. The meridional component is handled similarly. Then, $\overline{\mathbf{u}_{\mathrm{ag}}} \cdot \nabla_b Q^{\#}$ is calculated with a five point stencil and integrated exactly as $\overline{\mathbf{u}_g} \cdot \nabla_b Q^{\#}$.

We could compute the $w^{\#}$ advection integral directly using (43) and (40b), which yields

$$\begin{aligned} w^{\#}{Q^{\#}}_z = \overline{\boldsymbol{\omega}} \cdot \nabla(\overline{\mathbf{v}} \cdot \nabla\overline{b}) + \nabla\overline{b} \cdot \nabla \times (\overline{\boldsymbol{\omega}} \times \overline{\mathbf{v}}) \\ - (\overline{\mathbf{u}_g} + \overline{\mathbf{u}_{\mathrm{ag}}}) \cdot \nabla_b Q^{\#}, \end{aligned} \qquad (46)$$

but this merely reduces (45) to (42) once the (curl of the) complete momentum equation (25) and the complete buoyancy equation (37) are recognized and canceled, and therefore exposes $w^{\#}Q^{\#}_z$ to errors from the in-surface geostrophic PV advection, described above. Instead, we obtain the $w^{\#}Q^{\#}_z$ term in (45) as the residual.[3]

Almost indistinguishable results were obtained using other integration methods, e.g., assuming G and $|\overline{\mathbf{u}_g}|$ (rather than $G|\overline{\mathbf{u}_g}|^{-1}$) both vary linearly between contour points, which entails integration of G over the time required for the geostrophic flow to travel the distance ds.

c. Results

Figure 3 presents the results of the above integrations, forming the basis for the following discussion. Figures 4–6 provide supporting information, mapping $Q^{\#}$ forcings across the Southern Ocean, around Drake Passage, and on meridional sections, respectively.

Integrating the geostrophic $Q^{\#}$ advection along streamlines gives a reconstruction of $Q^{\#}(s)$ (gray), which closely matches the true $Q^{\#}(s)$, capturing its small-scale features and large-scale structure—except for near topography such as Kerguelen Plateau (~70°E), Campbell Plateau (~170°E), and Drake Passage (~60°W), where one extreme $Q^{\#}$ value can spoil the reconstruction. Generally though, advection errors caused by numerical discretization are small.

---

[3] To be clear, this does not mean that the $w^{\#}Q^{\#}_z$ term being nonzero is an indication of any failure to close the streamwise PV budget, (45). Rather, taking the $w^{\#}Q^{\#}_z$ term as a residual of (45) ensures that the contribution of geostrophic advection ($\overline{\mathbf{u}_g} \cdot \nabla_b Q^{\#}$) to $w^{\#}Q^{\#}_z$ in (46) does not accumulate discretization errors, but rather it satisfies (42) exactly.

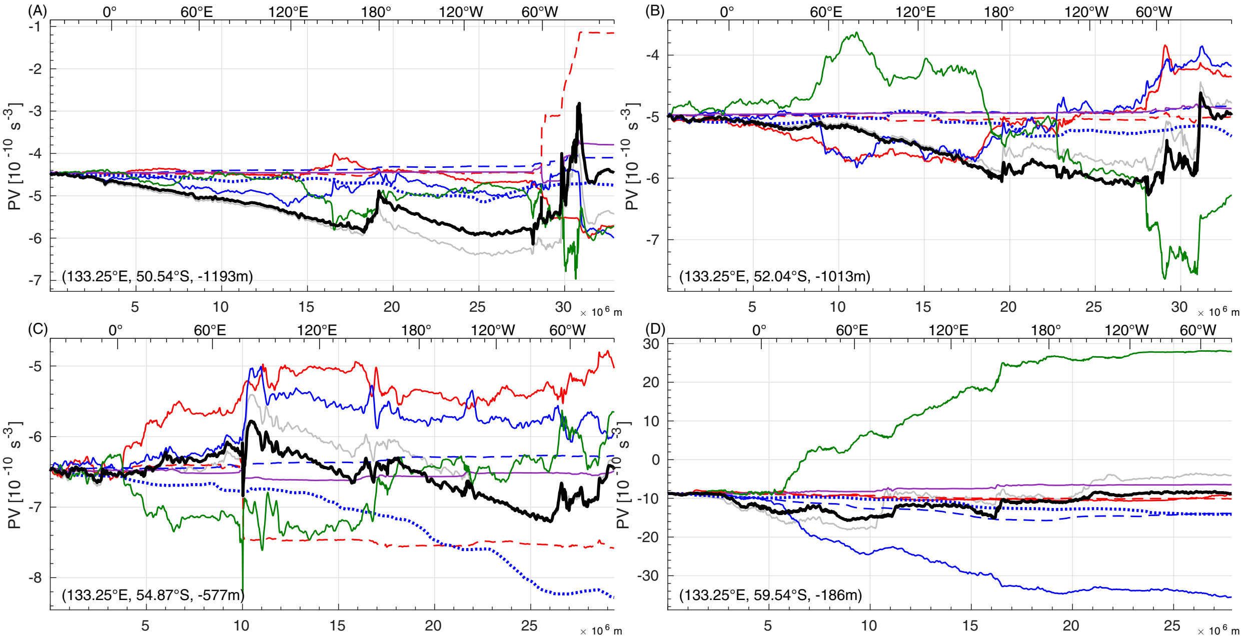

FIG. 3. $Q^\#$ (black) and its integrated forcing (colors) along the same four streamlines as in Fig. 2, starting from 40°W. The integrated forcings derive from ageostrophic advection (purple), buoyancy drift (dotted blue), eddy buoyancy fluxes (solid blue), buoyancy forcing (dashed blue), $w^\#$ advection (green), momentum drift (not shown, being negligible), eddy momentum fluxes (solid red), and momentum forcing (dashed red), in order from top to bottom then left to right on the RHS of (45). Also shown is the integrated geostrophic advection of $Q^\#$ [light gray, RHS of (42)], which should match $Q^\#$ (black), apart from advection errors caused by numerical discretization.

On the southernmost streamline D, $Q^\#(s)$ is fairly well conserved relative to its integrated forcings. The dominant forcings are the $w^\#$ advection (green) that increases $Q^\#$, and eddy buoyancy fluxes (solid blue) that decrease $Q^\#$. This streamline is consistently in a region of Ekman upwelling (Fig. 1a), which increases $Q^\#$ by advecting deeper, higher $Q^\#$ (lower $|Q^\#|$) water up onto the buoyancy surface. Though this heuristic argument is helpful, the relevant vertical advection is not the Ekman upwelling velocity, but rather is $w^\#$ which is heavily modified by the eddy field. Nonetheless, $w^\#$ is more positive than negative in this region (not shown), so $-w^\# Q^\#_z > 0$ since $Q^\#_z < 0$; by (45), $w^\#$ advection forces $Q^\#$ to increase along this and other southerly streamlines. This is opposite to the mechanism proposed by Gille (1997) that Ekman upwelling squeezes isopycnals toward the surface and decreases $Q^\#$ (increases $|Q^\#|$). Gille's (1997) proposed mechanism is rather Lagrangian in nature: $Q^\#$ supposedly decreases as isopycnals rise because it is measured rising with the isopycnals. Since our (and Gille's) analysis framework is Eulerian, so must be our interpretation: $Q^\#$ at a fixed point will increase as upwelling causes isopycnals to rise past this point, which now resides in less stratified water originating from below. Returning to the dominant balance, the $w^\#$ upwelling is largely counterbalanced by an eddy-induced downwelling, bringing low $Q^\#$ water from above down onto the buoyancy surface, and predominantly captured by the eddy buoyancy flux divergence in our Eulerian framework.

On streamline C, $w^\#$ advection causes $Q^\#$ to decrease, at least between Drake Passage and Kerguelen. Here, there is notable Ekman downwelling even on this reasonably southerly streamline, heuristically consistent with $w^\# < 0$ and $Q^\#$ decreasing. As above, eddies act to oppose the $w^\#$ forcing, though here eddy momentum fluxes (solid red) also contribute strongly. This may be surprising, given that $Q^\#$ is very well approximated by the thin-film PV, $f\overline{b}_z$, the budget of which does not contain eddy momentum forcing. Essentially, variations of vorticity (parallel to $\nabla\overline{b}$) are quickly converted into stratification variations, thereby maintaining a small Rossby number.

Downstream of Kerguelen, streamline C is more clearly in a region of Ekman upwelling, heuristically consistent with $w^\#$ forcing $Q^\#$ to increase, although interpretation in this region is challenged by the fact that buoyancy drift (dotted blue) becomes a major driver of $Q^\#$ loss downstream of Kerguelen. Indeed, buoyancy drift does not generally dominate the $Q^\#$ budget in any single water column (except in the far south, where the buoyancy surface is near the sea surface), but it is single-signed over vast regions, so can integrate to a considerable forcing (Fig. 4a). Finally, though momentum forcing (dashed red) is generally insignificant as a driver of $Q^\#$, close encounters with topography can lead to massive and rapid $Q^\#$ forcing by frictional drag, as at ~70°E where streamline C passes just north of Kerguelen Plateau, and sidewall drag exerts a negative torque on the fluid, decreasing $Q^\#$. The frictional forcing of PV is a robust feature along topography

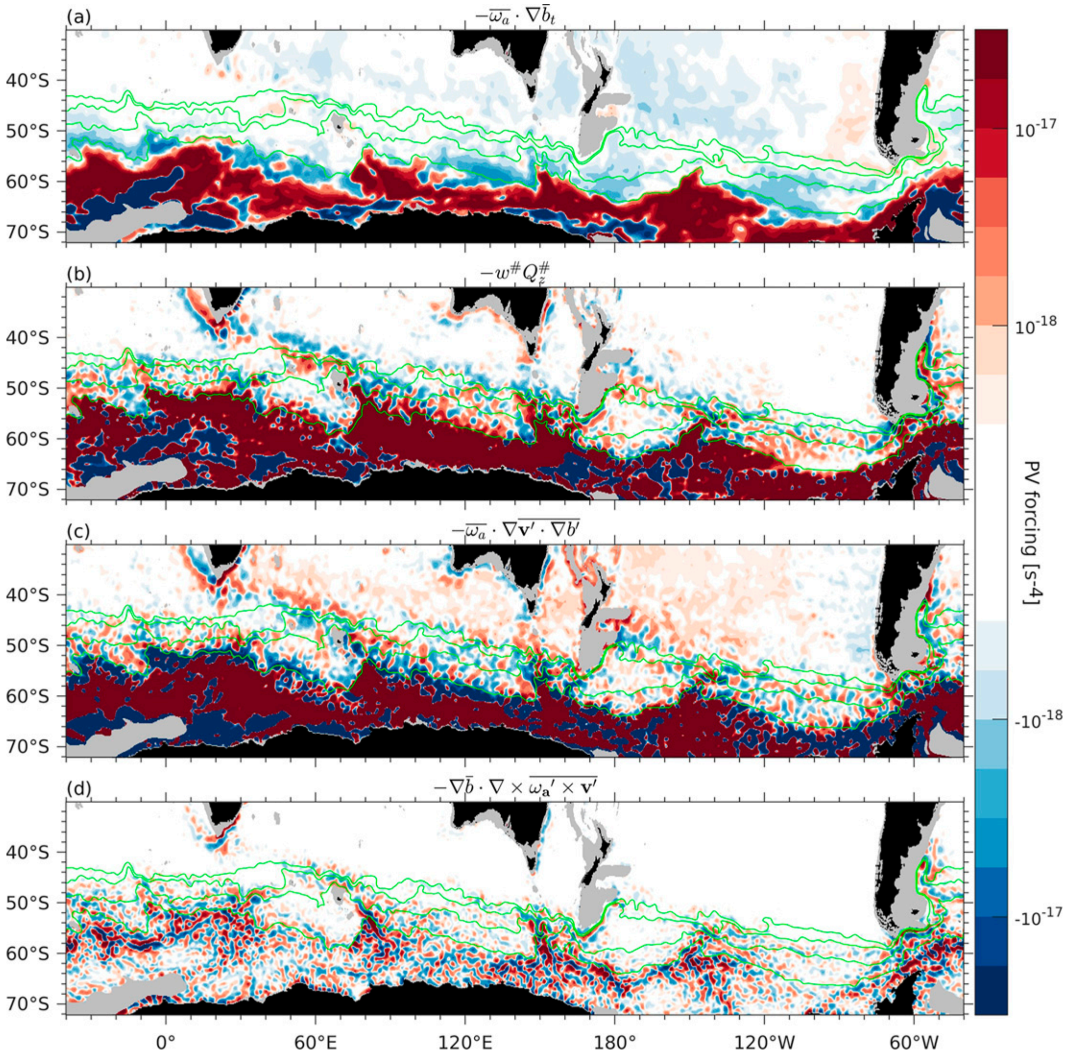

FIG. 4. Maps of selected PV forcing terms (s^{-4}) deriving from (a) the buoyancy tendency, (b) the $w^{\#}$ advection, (c) the eddy buoyancy flux, and (d) the eddy momentum flux. Their signs are as in (45), so $Q^{\#}$ increases following the geostrophic flow through red regions. For presentation, these maps are smoothed by a mean-preserving Gaussian filter with 2/3° zonal standard deviation and 1/3° meridional standard deviation. Light gray indicates where the mean buoyancy surface has incropped or outcropped. The four streamlines in Fig. 2 and Fig. 3 are shown in green.

(Fig. 5e); it is not due to one malicious grid point, though it appears so from the zoomed-out view of Fig. 3c.[4]

Along streamline B, eddy forcing—of both buoyancy and momentum—force $Q^{\#}$ to decrease in the Indian sector from ~20° to ~170°E, opposed by $w^{\#}$ advection. This region contains the Dynamical Subtropical Front, which (unlike the Subtropical Front) is also a deep water mass boundary (Graham and De Boer 2013). This front is seen clearly as a dipolar structure in the Indian sector of Figs. 4b and 4c, where eddy buoyancy fluxes cause $Q^{\#}$ to decrease on the southern side of the dipole, and to increase on the northern side—as predicted in section 2g—while $w^{\#}$ advection does the opposite. In fact, $Q^{\#}$ actually decreases northward here (Fig. 1b), suggesting that the $w^{\#}$ advection establishes this northward $Q^{\#}$ decrease, while eddy forcing erodes it, homogenizing PV as eddies that flux PV downgradient do. Indeed, this region exhibits relatively homogeneous PV (Stanley et al. 2020, their Fig. 8). Along this front, mean buoyancy surfaces rise steeply poleward (Figs. 6a,c), lifted in the south and depressed in the north by Ekman suction/pumping (Fig. 1a). Through baroclinic instability, mesoscale eddies oppose this, fluxing buoyancy poleward across the front, creating a dipolar structure to the eddy buoyancy flux divergence. Moreover, this divergence increases in magnitude moving up the water column until ~300-m depth (Fig. 6a), broadly consistent with the vertical structure of the fastest growing baroclinic modes (Smith 2007). Thus, on the

---

[4] The discretization of appendix A was crucial to obtain accurate analysis this close to topography.

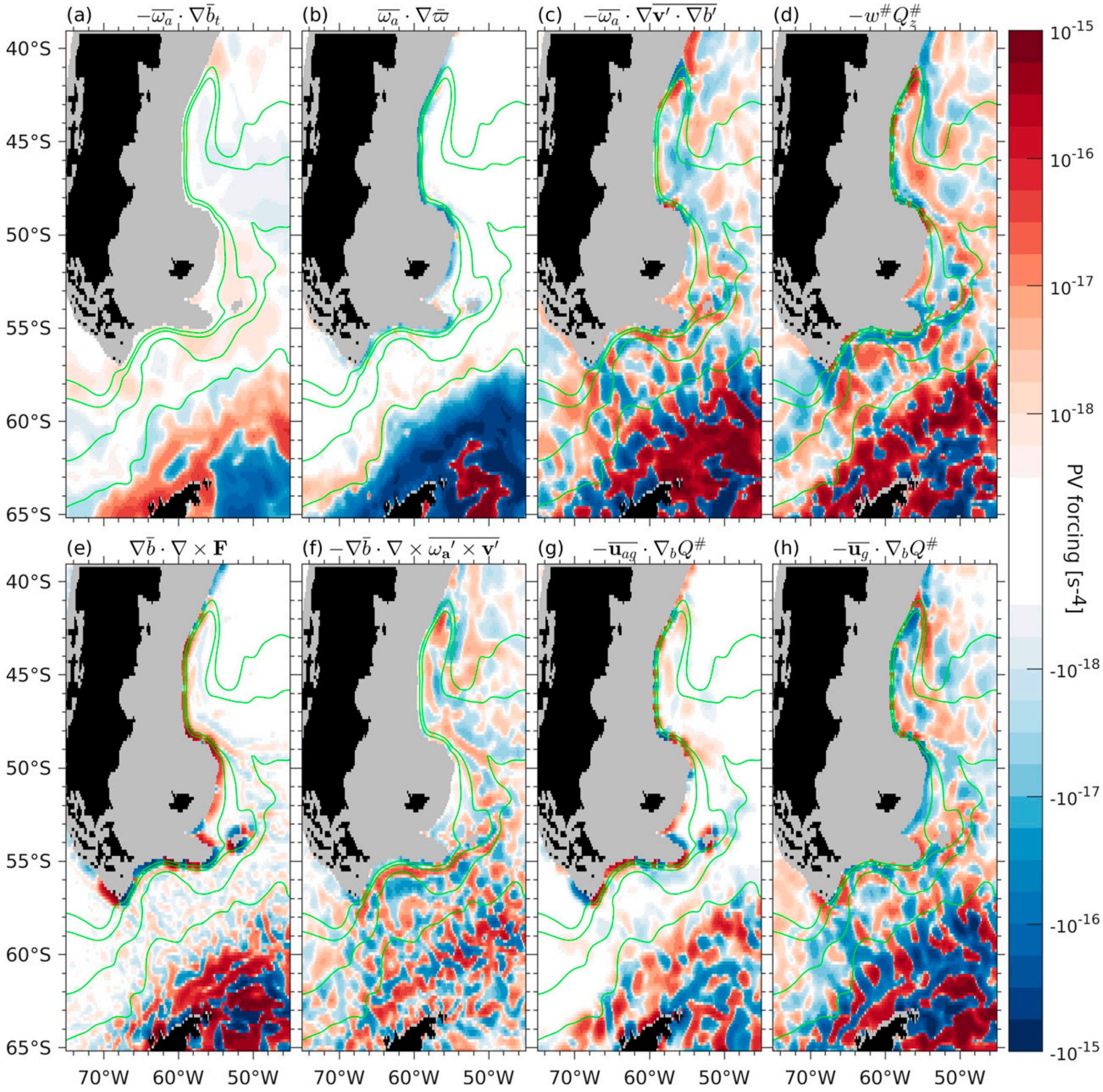

FIG. 5. As in Fig. 4, but zoomed into the Drake Passage region and showing all PV forcings, deriving from (a) buoyancy tendency, (b) buoyancy forcing, (c) eddy buoyancy flux, (d) $w^{\#}$ advection, (e) momentum forcing, (f) eddy momentum flux, (g) ageostrophic advection, and (h) geostrophic advection. For presentation, these maps are smoothed by a mean-preserving Gaussian filter with 1/3° zonal standard deviation and 1/6° meridional standard deviation.

southern flank of this front at middepths, $-\overline{\mathbf{v}'\cdot\nabla b'} > 0$ lightening waters, and $-\overline{\boldsymbol{\varpi}}\cdot\nabla\overline{\mathbf{v}'\cdot\nabla b'} \approx -f(\overline{\mathbf{v}'\cdot\nabla b'})_z < 0$ forcing $Q^{\#}$ to decrease. Put another way, mesoscale eddies tend to flatten isopycnals, largely by means of an eddy-induced velocity $\mathbf{v}^*$ that is downward on the southern flank, advecting low $Q^{\#}$ water onto the buoyancy surface and materially decreasing $Q^{\#}$ (with the reverse occurring on the northern flank). Streamline B transits through the south flank of the Dynamical Subtropical Front (Figs. 4b,c and 6a,c), and so encounters eddy forcing that materially decreases $Q^{\#}$.

This balance for streamline B reverses in the Pacific sector, where eddy forcing increases $Q^{\#}$ and $w^{\#}$ advection decreases $Q^{\#}$. While the dipolar structure of the Dynamical Subtropical Front is less clear in the Pacific sector, there is evidently still a net signal of eddy-induced upwelling that increases $Q^{\#}$, even in the eastern Pacific where eddy buoyancy forcing of $Q^{\#}$ appears more noisy and eddy-like (Fig. 4c). This is typical of the Drake Passage latitudes, with Ekman pumping counterbalanced by eddy-induced upwelling. Streamline B is northerly enough that it escapes this regime in the Indian sector, but

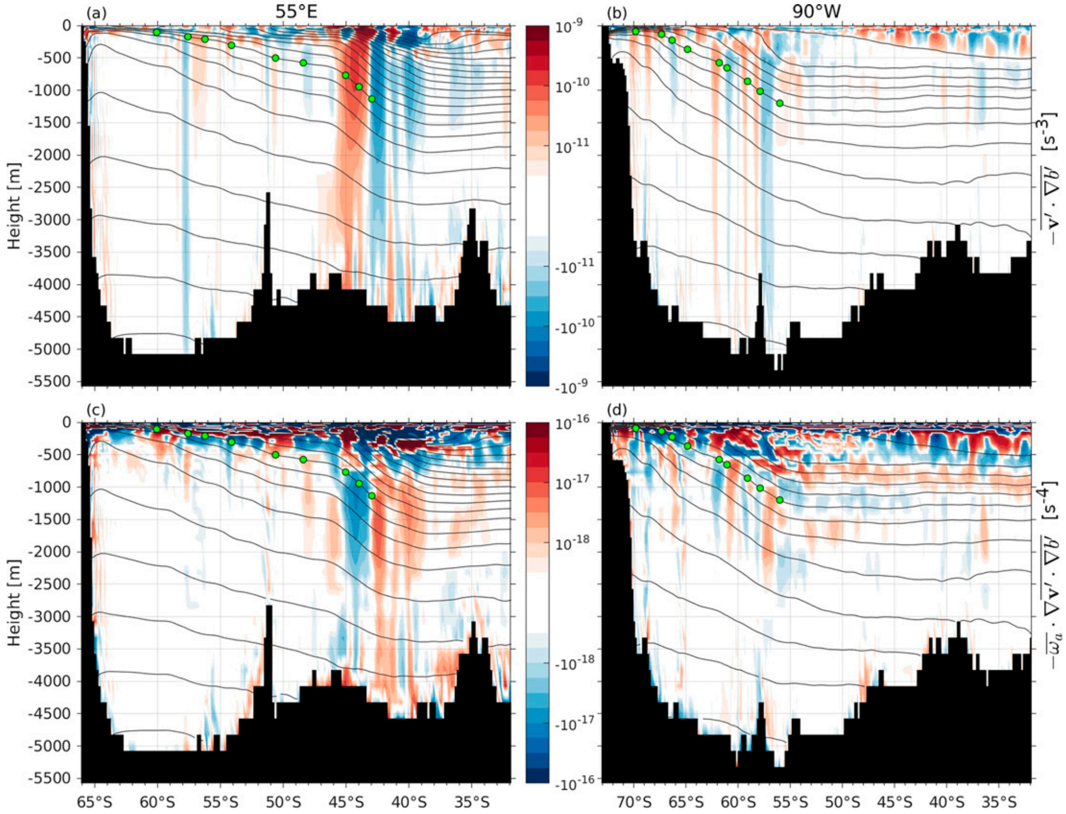

FIG. 6. Meridional sections of (top) the eddy buoyancy flux and (bottom) its contribution to the $Q^\#$ budget, centered at (left) 55°E and (right) 90°W and zonally averaged over 0.5°. Green dots indicate where the nine streamlines from Fig. 1 intersect the meridional section. Buoyancy surfaces are contoured every 10^{-3} m s^{-2}, up to the buoyancy value at the surface of the northernmost streamline.

must inhabit this regime in the Pacific sector in order to pass through Drake Passage.

Where streamline B flows northward along Campbell Plateau and the Argentine slope, eddy buoyancy and momentum forcing both cause $Q^\#$ to increase. Usually, the ACC's eastward flow is sufficiently strong that eddies are advected eastward (Hughes 1995; Hughes et al. 1998; Klocker and Marshall 2014). With the flow deflected northward here, eddies can propagate west [see Fig. 3.1 of Zajaczkovski (2017), or Fig. 1c of Klocker and Marshall (2014)], impinging on the continental slope where they break—largely by transferring energy into high wavenumber vertical modes (Dewar and Hogg 2010)—and form an "eddy graveyard" (Zhai et al. 2010). These breaking eddies strongly force the PV, generally causing $Q^\#$ to increase and enabling the northward flow in a self-supporting cycle.

Streamline A is the northernmost circumpolar streamline, passing very close to the Argentine slope. Here, the dramatic $Q^\#$ gain is driven overwhelmingly by momentum forcing, where the northward flow along a no-slip western boundary induces a positive torque on the fluid, increasing $f + \zeta$, and $Q^\#$. Again, this frictional forcing is a robust signal, with large and generally positive $Q^\#$ forcings along the Argentine slope (Fig. 5e).

Away from Drake Passage and Campbell Plateau, the steady decrease of $Q^\#$ along streamline A is driven by a complicated combination of eddy buoyancy and momentum fluxes and $w^\#$ advection, not to mention buoyancy drift. These signals are subtler than for streamline B because streamline A threads between the large dipolar structure of $Q^\#$ forcings by eddy buoyancy fluxes and $w^\#$ advection in the Indian sector (Figs. 4b,c and 6c). Noting that the net $Q^\#$ eddy forcing in the Pacific sector is not as strong and coherent as in the Indian sector (Figs. 4b,c and 6c,d), we hypothesize that streamline A cannot pass any further north than it does while remaining circumpolar: if streamline A inhabited the northern flank of the Subtropical Dynamical Front, eddy buoyancy fluxes would strongly force $Q^\#$ to increase there, opposite to the $Q^\#$ decrease that is required to counterbalance the rise of $Q^\#$ that robustly occurs along the Argentine slope. The usual coarse-grained view of the Southern Ocean's residual overturning circulation involves mean (Ekman) upwelling and eddy-induced downwelling in the southern reaches of the ACC, and the reverse in the northern reaches. However, finer-resolution inspection reveals that isopycnals are steeper in the Dynamical Subtropical Front than in the rest of the ACC further south (Fig. 6a), leading to an eddy buoyancy flux convergence and eddy-induced downwelling on the southern flank of this front,

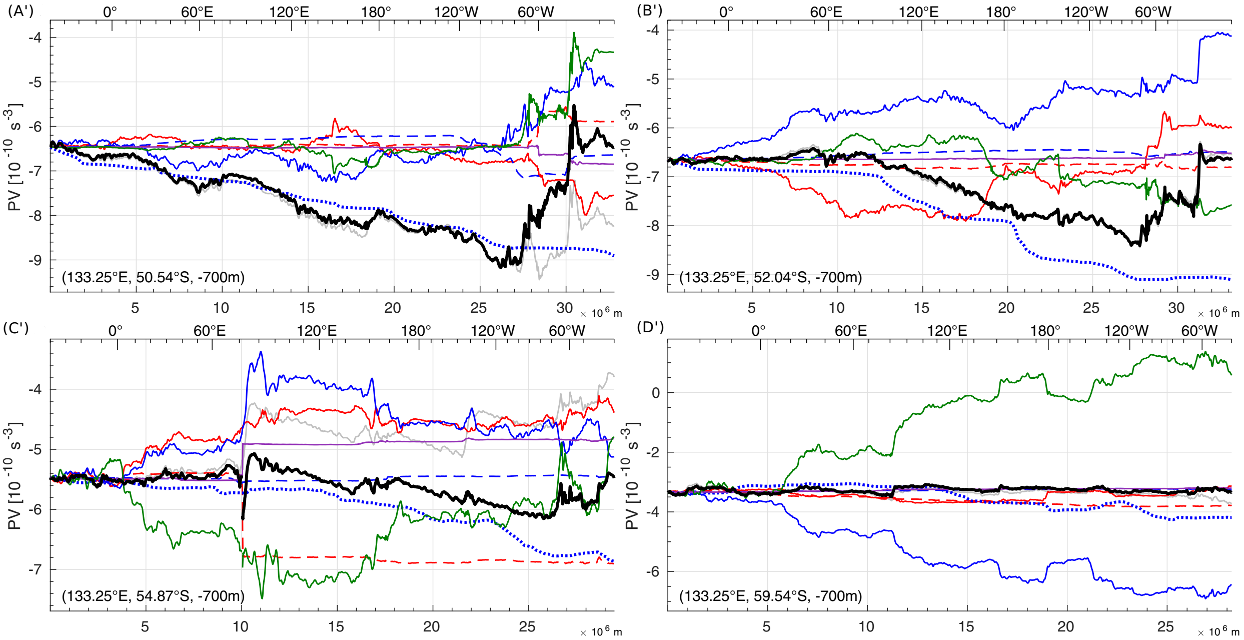

FIG. 7. As in Fig. 3, but for streamlines on different buoyancy surfaces, all intersecting 133.25°E at −700 m.

even though this lies in the northern reaches of the ACC. If we define the northern limit of the ACC to be the northernmost circumpolar (geostrophic) streamline, then the northern limit of the ACC—at least in the Indian sector—is actually the southern flank of the Dynamical Subtropical Front, where mean upwelling and eddy-induced downwelling occur.

For all streamlines, diapycnal forcing of $Q^{\#}$ (dashed blue) is generally small, in agreement with Gille (1997), though not insignificant for streamline D, it being relatively shallow. Our choice of in situ density anomaly to define buoyancy and our numerics ensure the solenoidal term is precisely zero, whereas Gille (1997) used potential density and found the solenoidal term a major PV forcing (her Fig. 7b). We repeated our numerical methods using potential density and found the solenoidal PV forcing becomes nonzero but remains negligible, meaning the large solenoidal forcing Gille (1997) found is due to her numerics, not inherent issues with potential density. Gille (1997) also found buoyancy and momentum forcing is a dominant PV forcing even away from topographic boundaries, whereas we find these terms are negligible in the ocean interior; this difference is likely an artifact of the lower-resolution Semtner–Chervin model analyzed by Gille (1997).

Ageostrophic advection is generally insignificant at forcing $Q^{\#}$, except near topographic obstacles. The dramatic rise of $Q^{\#}$ along streamline A at Drake Passage, for example, is driven partly by ageostrophic advection (purple). Indeed, some geostrophic streamlines intersect South America, therefore requiring relatively strong ageostrophic flow to navigate Drake Passage. High $Q^{\#}$ water originating north of the ACC is ageostrophically advected onto streamline A, increasing $Q^{\#}$. Real fluid parcels do not follow the mean streamlines, geostrophic or otherwise. If a fluid parcel transiting Drake Passage is better at conserving its PV than fluid following the streamlines, its $Q^{\#}$ will rise less at Drake Passage and consequently will migrate southward across streamlines. This is consistent with the residual meridional overturning circulation taking water, particularly in the Atlantic sector, across the ACC from north to south at these middepths, as water “spirals in” toward Antarctica (Tamsitt et al. 2017). However, this effect of ageostrophic advection forcing $Q^{\#}$ to increase at Drake Passage is not robust, as other streamlines exhibit the opposite tendency (Fig. 7a). Indeed, the ageostrophic forcing of $Q^{\#}$ in the Drake Passage region is rich and complex (Fig. 5g). In the southern ACC however, ageostrophic forcing of $Q^{\#}$ appears to be more placid, creating a small but steady rise of $Q^{\#}$ along streamline D, again consistent with poleward ageostrophic flow on this surface.

To examine the sensitivity of these results to the particular depth of the surface, we repeat the analysis along four new streamlines—labeled A′, B′, C′, and D′—that intersect 133.25°E at −700 m height, regardless of latitude (Fig. 7). Each such streamline exists on a different buoyancy surface, so we choose reference S_0 and θ_0 local to where each streamline intersects (133.25°E, −700 m), and recalculate all quantities. The dominant balance along streamline D′ is the same as that for streamline D, despite the latter being far shallower (generally at 150 to 250 m depth). Likewise, the results along streamline C′ are qualitatively unchanged, as expected since streamline C intersected (133.25°E, −54.87°S) at −577 m, not far from −700 m. Further analyses of $Q^{\#}$ forcing along streamlines A′ and B′ are withheld, owing to the dominant effect of buoyancy drift around 700 m depth in the ACC during the SOSE record. This is not particular to Eulerian averaging, but also arises under TWA averaging (Fig. C1). This dominant buoyancy drift is also seen in gridded Argo data (not shown, but expected since SOSE incorporates Argo).

6. Conclusions

The wind stress curl over the Southern Ocean lifts up deep, dense water through Ekman suction and drives poleward Sverdrup flow that, in the latitudes north of Cape Horn, is balanced by an equatorward-flowing western boundary current along the Argentine slope. However, this is not a classic subpolar gyre, since the boundary current is fed not by westward drift, but by the circumpolar current itself (Stommel 1957). In the Drake Passage latitudes where there are no continental barriers, the poleward Sverdrup flow is instead balanced by a richly heterogeneous but net equatorward flow supported by bottom pressure torque. That is, the bottom pressure torque is a dominant term in the barotropic vorticity budget, balancing wind stress curl in the net. This is linked, as Hughes and De Cuevas (2001) made clear, to bottom form drag (the curl of which is the bottom pressure torque) being the dominant sink of easterly momentum input by the wind stress in the barotropic momentum budget.

Moving from barotropic to layerwise dynamics, eddies become of prime importance. The downward transfer of mean momentum from the surface to the bottom is overwhelmingly achieved by eddy form stress on sloping isopycnals, enabled by hundreds of mesoscale eddies that populate the ACC. It is well known that this process is accompanied by a mean poleward buoyancy transport (Johnson and Bryden 1989). We have shown that these related eddy processes are also accompanied by a material forcing of mean potential vorticity, driven by the curl of the eddy form stress. This is a dominant term in the mean potential vorticity budget, just as the eddy form stress is a dominant term in the mean layerwise momentum budget—analogous to the aforementioned link established by Hughes and De Cuevas (2001).

For a jet like the ACC (or its filaments) in the open ocean, this eddy PV forcing ideally takes a dipolar structure, acting at middepths to increase PV on the northern flank, and decrease PV on the southern flank. Meanwhile, as the ACC transits along the Argentine slope, PV is materially increased (toward zero), as shown by Gille (1997) and verified here. This material PV increase is driven by drag spinning down the current or, farther offshore, breaking eddies having the same effect.

Together, these two regimes create an apparent contradiction for fluid parcels recirculating along the northern flank of the ACC, as their PV would continually increase. One might argue that fluid parcels do not recirculate in the ACC, but rather migrate across closed streamlines. Given the material PV increase, however, such a migration would be equatorward, in contrast to the poleward migration at these middepths required to balance the water mass transformation into Antarctic Bottom Water. Regardless, such migration is slight, as ageostrophic forcing of mean PV along mean geostrophic streamlines is almost negligible compared to eddy or near-boundary PV forcing. Instead, the ACC resolves this contradiction by merging with the subtropical gyres to the north, creating an eddy-rich jet for which the northernmost Antarctic Circumpolar Current's streamlines inhabit the jet's southern flank, where PV decreases. The PV decrease thus accumulated in the open ocean is able to balance the PV increase as circumpolar streamlines transit along the Argentine slope.

The length of the ACC's northward excursion along the Argentine slope may therefore be dynamically controlled by this requirement for the ACC to merge with the subtropical gyres. Since the length of this northward ACC excursion (as the Malvinas Current) determines the latitude of the Brazil/Malvinas Confluence (BMC), this suggests a new mechanism by which remote factors can influence the BMC latitude: more (or less) eddy-driven PV loss along ACC streamlines in the open ocean must be balanced by longer (or shorter) northward ACC excursions along the Argentine slope. Though a complete theory for the BMC latitude is still lacking, this mechanism may play a role alongside other factors such as the relative transports of the Brazil and Malvinas Currents (Matano 1993) and the latitude of the maximum wind stress curl (Lumpkin and Garzoli 2011). Such dynamic constraints may control the mean BMC latitude as well as its fluctuations on decadal time scales—for which there appears to be a recent southward trend (Lumpkin and Garzoli 2011; Combes and Matano 2014)—while fluctuations of the BMC latitude on shorter time scales appear to be driven by Rossby waves (Bodnariuk et al. 2021). In these matters, care must be taken to distinguish between the latitude of separation from the continental slope and the more southerly latitude at which the BMC settles offshore; between these latitudes the Malvinas Current is overshooting, enabling further PV gain along the continental slope. This hypothesis, by which remote eddy PV forcing on the northern flank of the ACC influences the BMC latitude, remains speculative and requires further research. One implication of this hypothesis is that the BMC latitude may be different between coarse-resolution and eddy-resolving models. An intriguing and possibly related question regards why the eddy PV forcing appears, in SOSE, to most coherently exhibit the aforementioned dipolar structure with axis parallel to the jet in the Indian sector, and least in the Atlantic sector.

These two regimes of the mean PV structure along mean streamlines of the northern ACC—decreasing in the open ocean and increasing downstream of Drake Passage—are robust signals, regardless of whether the averaging is Eulerian or semi-Lagrangian (following buoyancy surfaces as in TWA).

In the Eulerian perspective, the open-ocean PV increase is framed as the near but not exact cancelation of the mean Ekman overturning circulation by an eddy-induced overturning cell. On the northern flank of a jet, the mean and eddy-induced overturning circulations respectively advect low (large and negative) and high (near zero) PV from above and below, acting to materially decrease or increase PV. The reverse holds on the southern flank. The eddy PV forcing slightly outcompetes the mean PV advection, producing a remarkably steady decrease of PV along mean northern circumpolar streamlines in the open ocean, particularly in the Indian sector.

Under a TWA analysis, wherein the residual circulation of the Southern Ocean is naturally captured, the two dominant but counterbalancing PV forcings of the Eulerian PV budget would, we expect, coalesce into a single dominant PV forcing due to eddy form stress, at least in the ocean interior. Close to boundaries, other TWA PV forcings such as due to friction and ageostrophic advection will be significant, as in the Eulerian PV budget.

As Gille (1997) pointed out, this nonconservation of mean PV along mean streamlines bears on many theoretical models of the ACC. For instance, the equivalent barotropic structure of Killworth (1992) relies on a functional relationship between PV and the mass-weighted streamfunction on layers, which is broken by this nonconservation of mean PV. Going one step further, Marshall (1995) assumed that PV is uniform on layers. This assumption is one (probably major) reason why his modeled ACC does not veer northward downstream of Drake Passage, as the real ACC does: with PV uniform, his flow can only move northward by shrinking the layer thickness, upon which mass conservation puts strong limits. Such models are intended only to capture the first-order dynamics of the ACC, and hence can be quite tractable and illuminating. However, given the dominant role of eddy PV forcing and that mean PV can vary by ~50% along a mean streamline—not to mention variations across streamlines (Stanley et al. 2020)—we argue that PV-conserving flow should not be considered as the ACC's first-order dynamics. Rather, nonconservation of PV is a first-order effect.

Several multibasin idealized models have recently coupled global oceanic processes—notably convective downwelling in the North Atlantic and diffusive upwelling predominantly in the Pacific—through the Southern Ocean with simplified ACC dynamics (Thompson et al. 2016; Jones and Cessi 2016). To geostrophically support a mass transfer of intermediate waters from the Pacific to Atlantic (and vice versa of deep waters), these models require a difference of PV between the Atlantic and Pacific sectors. As this PV difference is established by eddy and boundary PV forcings, further work with such models that brings PV forcing to the forefront of ACC dynamics may prove enlightening.

Acknowledgments. We thank Ed Doddridge, Ryan Holmes, Chris Hughes, Matt Mazloff, Trevor McDougall, Jan Zika, and two reviewers for helpful discussions. GJS acknowledges partial support from the Clarendon Fund and the Canadian Alumni Scholarship at Linacre College, Oxford, and from the Australian Research Council though Grant FL150100090. DPM acknowledges the partial support of the Natural Environment Research Council, NE/R000999/1.

Data availability statement. SOSE output is available at http://sose.ucsd.edu.

APPENDIX A

Numerical Methods

Careful numerical methods are required to study the structure and forcing of PV along streamlines. SOSE uses an Arakawa C-grid (Arakawa and Lamb 1977): u, v, and w live on the west, south, and upper faces of the tracer cell, respectively, while vertical vorticity (f and ζ) lives on the southwest edge of the tracer cell.

a. Buoyancy

To calculate the time-mean buoyancy from (22) requires the time-mean density, but nonlinearities in R cause $\overline{\rho} \neq R(\overline{S}, \overline{\theta}, -g\rho_c z)$. Instead, we invert hydrostatic balance in each water column to obtain the in situ density ρ_k from the known pressure p_k and height z_k at each model level k, starting with

$$p_1 = g\rho_c \eta - g\rho_1 z_1, \tag{A1}$$

where η is the sea surface height, and continuing for $k > 1$ with

$$\frac{p_k - p_{k-1}}{z_k - z_{k-1}} = -g\frac{\rho_{k-1} + \rho_k}{2}. \tag{A2}$$

This is equally valid for 5-day or 6-yr means.

Next, we select the reference values S_0 and θ_0, which should be chosen close to S and θ found in one's study region to make the buoyancy surface close to neutral. We simply choose a reference location (x_0, y_0, z_0) and define $S_0 = \overline{S}(x_0, y_0, z_0)$ and $\theta_0 = \overline{\theta}(x_0, y_0, z_0)$. Then, $\overline{b}$ is calculated from (22) with ρ replaced by $\overline{\rho}$.

This buoyancy variable can exhibit overturns, which we simply and effectively deal with by sorting $\overline{b}$ in the vertical dimension. Since the overturns are rare and mostly in the mixed layer, this does not impact our analysis on an interior buoyancy surface. In contrast, Uchida et al. (2021) ensured b is monotonic in z by choosing their reference density profile as the vertical integral of a virtual compressibility, itself chosen as a function of height to be the minimum compressibility in their domain at each height. Their buoyancy variable therefore has $b_z \geq N^2$ (with equality at one point for each height, where their surface is neutral) leading to surfaces that are systematically inclined away from the neutral tangent plane and toward geopotentials, and hence are less neutral than our prescription. Essentially, the contribution of vertical variations of S and θ to vertical variations of in situ density—which Uchida et al. (2021) missed in their Eq. (4)—means the virtual compressibility should be allowed to exceed the true compressibility in roughly half the ocean, such that $b_z \approx N^2$.

The isovalue of our buoyancy surface is $b_0 = \overline{b}(x_0, y_0, z_0)$, where the RHS is evaluated by linearly interpolating $\overline{b}(x_0, y_0)$ as a function of z. Likewise, the height of our surface, $\xi^\#(x, y, b_0)$, is obtained by linear interpolation of z as a function of $\overline{b}$ in each water column (x, y) to b_0. Hence, $\xi^\#(x_0, y_0, b_0) = z_0$. Note $b_0 \approx 0$ m s^{-2} but not exactly because of nonlinearities in R.

b. Geostrophic streamfunction

To evaluate $\overline{m}$ on the $\overline{b} = b_0$ surface, simply evaluate $\overline{m}$ at height $\xi^\#$:

$$\overline{m}_0(x, y) = \overline{m}(x, y, \xi^\#(x, y, b_0)). \tag{A3}$$

Numerically, we use trapezoidal integration in (41), consistent with obtaining $\xi^\#$ by linear interpolation of $\overline{b}$ to b_0. We use $z_1 = -5$ m, the height of the shallowest tracer cell center.

We desire the streamline of $\overline{m}_0(x, y)$ through (x_0, y_0), but in general the level set of $\overline{m}_0(x, y)$ on the value $\overline{m}_0(x_0, y_0)$ consists of several disjoint components. To select the desired streamline, we create $\overline{M}_0(x, y)$ equal to $\overline{m}_0(x, y)$ but with incrops or outcrops filled with (i) $+\infty$ where adjacent to the African, Australian, and American continents, (ii) $-\infty$ where adjacent to Antarctica, and (iii) $\overline{m}_0(x_0, y_0)$ elsewhere. We select the contour (a connected component of a level set) of $\overline{M}_0$ through (x_0, y_0)—this is guaranteed to be circumpolar—then remove all filled data points from this contour. This yields a circumpolar streamline of $\overline{m}_0(x, y)$ through (x_0, y_0) that may consist of multiple disjoint contours.

c. Ertel–Euler PV budget

To close the time-mean momentum budget, we use model outputs for $\overline{\mathbf{u}_t}$, $\overline{\mathbf{F}}$, $\overline{w\mathbf{u}_z}$, $f\widehat{\mathbf{k}} \times \overline{\mathbf{u}}$, $\overline{\zeta\widehat{\mathbf{k}} \times \mathbf{u}}$, and $\overline{\nabla_z(u^2 + v^2)/2}$. The sum of the last three of these terms is $\overline{\boldsymbol{\omega} \times \mathbf{v}}$ up to a conservative vector field $\nabla\overline{K}$, which the curl in (38) annihilates. We then compute $\overline{w}\,\overline{\mathbf{u}}_z$, $\overline{\zeta}\widehat{\mathbf{k}} \times \overline{\mathbf{u}}$, and $\nabla_z(\overline{u}^2 + \overline{v}^2)/2$ using the same numerical scheme that SOSE uses for the analogous instantaneous accelerations. We get the eddy terms $\overline{w'\mathbf{u}'_z}$, $\overline{\zeta'\widehat{\mathbf{k}} \times \mathbf{u}'}$, and $\nabla_z\overline{(u'^2 + v'^2)/2}$ as residuals: $\overline{w'\mathbf{u}'_z} = \overline{w\mathbf{u}_z} - \overline{w}\,\overline{\mathbf{u}_z}$, etc. Again, the sum of these three eddy advection accelerations equals $\overline{\boldsymbol{\omega}' \times \mathbf{v}'}$ for use in (39), up to a conservative vector field.

The time-mean buoyancy budget cannot be determined purely from time-mean quantities, because of nonlinearity in R. Instead, for each 5-day mean, we calculate b_t, $\mathbf{v} \cdot \nabla b$, and $\boldsymbol{\varpi}$ via (30). We average these to obtain $\overline{b_t}$, $\overline{\mathbf{v} \cdot \nabla b}$, and $\overline{\boldsymbol{\varpi}}$. Finally, we compute $\overline{\mathbf{v}} \cdot \nabla\overline{b}$ using SOSE's tracer advection scheme (third-order upwind space and time centered), and get the eddy buoyancy advection as a residual: $\overline{\mathbf{v}' \cdot \nabla b'} = \overline{\mathbf{v} \cdot \nabla b} - \overline{\mathbf{v}} \cdot \nabla\overline{b}$.

Our numerical discretization is carefully designed to satisfy the vector identities $\nabla \cdot \overline{\boldsymbol{\varpi}} = 0$, $\nabla \times \nabla\overline{b} = 0$, $\nabla \cdot \overline{\mathbf{v}} = 0$ that underpin the PV advection (40b). We employ the divergence theorem and Stokes' theorem at each step. The vertical component of vorticity, $\zeta = v_x - u_y$, is computed using Stokes' theorem to exchange an area integral of ζ for a line integral of the circulation around the perimeter of the vertical vorticity cell centered on the southwest corner of the tracer cell (matching the model's numerics). We extend this analogously to compute the horizontal components of the vorticity. We average b onto these three vorticity grids, multiply by the vorticity components, integrate across the six faces of the vorticity cell centered on the upper southwest corner of the tracer cell, and divide by the vorticity cell's volume to obtain $Q^{\#} = \nabla \cdot (\overline{\varpi}\,\overline{b})$.

The above procedure calculates $(\nabla \times \mathbf{a}) \cdot \nabla T$ as $\nabla \cdot (T\nabla \times \mathbf{a})$ for any "staggered" vector field $\mathbf{a}$ (having components on the u, v, and w grids) and any scalar field (tracer) T. Hence, the same numerics that calculate $Q^{\#}$ naturally calculate its forcing terms in (39). For example, $T = \overline{b}$ and $\mathbf{a} = \overline{\boldsymbol{\omega}} \times \overline{\mathbf{v}}$ yields the PV advection, $\nabla\overline{b} \cdot (\nabla \times \overline{\boldsymbol{\omega}} \times \overline{\mathbf{v}})$. Alternatively, $T = \overline{\mathbf{v}' \cdot \nabla b'}$ and $\mathbf{a} = \mathbf{v}$ yields the eddy buoyancy forcing of PV, $-\overline{\boldsymbol{\omega}} \cdot \nabla(\overline{\mathbf{v}' \cdot \nabla b'})$, provided $\nabla \times \mathbf{a}$ is trivially augmented by $f\widehat{\mathbf{k}}$. Masking is handled naturally: any vorticity point with $Q^{\#}$ will also have valid $Q^{\#}$ forcings. This discretization ensures the solenoidal term $\nabla\overline{b} \cdot \nabla \times (-g\rho_c^{-1}\overline{\rho}\widehat{\mathbf{k}}) = 0$ identically.

We now have 3D data for $Q^{\#}$ and its forcings on the upper southwest corner of the tracer cells. We average $\xi^{\#}(x,\ y,\ b_0)$ four ways onto the southwest corner of the horizontal tracer grid, onto which we vertically interpolate $Q^{\#}$ and its forcings from the height of the w grid. This interpolation is linear, so the PV budget (39) that holds at each grid point also holds on the surface. Finally, $Q^{\#}$ and its forcings are horizontally interpolated to the contour points of each geostrophic streamline; these points live directly between two adjacent grid points of the geostrophic streamfunction, so this interpolation is linear (not bilinear).

APPENDIX B

Euler–Ertel and Thickness-Weighted Average PV

Here, we verify that the structure of the Ertel–Euler PV along mean geostrophic streamlines is a robust signature, insofar as it qualitatively matches with results using alternative definitions of PV and geostrophic streamlines.

a. Euler–Ertel PV

1) DEFINITION

The time-mean PV used by Gille (1997) is

$$\overline{Q^{\sigma_1}} = \overline{(f + \zeta)(\sigma_1)_z}, \tag{B1}$$

here called the "Euler–Ertel PV" because it is the Eulerian time-mean of the Ertel PV, albeit only the vorticity's vertical component is retained, and σ_1 (potential density referenced to 1000 dbar) is used instead of b from (22).

2) GEOSTROPHIC STREAMFUNCTION

No exact geostrophic streamfunction exists for potential density surfaces (McDougall 1989). Gille (1997) used the Zhang and Hogg (1992) generalization of the Montgomery (1937) potential, which references the surface's height to its mean value, thereby reducing errors in estimating the geostrophic velocity caused by variations of b on the σ_1 surface. Instead, we use the orthobaric Montgomery potential (Stanley 2019b), which references the surface's height to a value that depends on the local value of b on the σ_1 surface. This further generalizes the Zhang and Hogg (1992) streamfunction and further reduces errors.

3) NUMERICS

In contrast to $Q^{\#}$, we assemble Q^{σ_1} on the tracer cell center, in part to simultaneously assess the extent to which such gridding issues affect the PV structure along streamlines. We calculate σ_1 from 5-day means of S and θ, from which we build $\overline{\sigma_1}$. We get $(\sigma_1)_z$ by finite difference on the w grid, then average back to the tracer grid. We calculate ζ from 5-day means of u and v as in appendix A, section c, then average ζ onto the

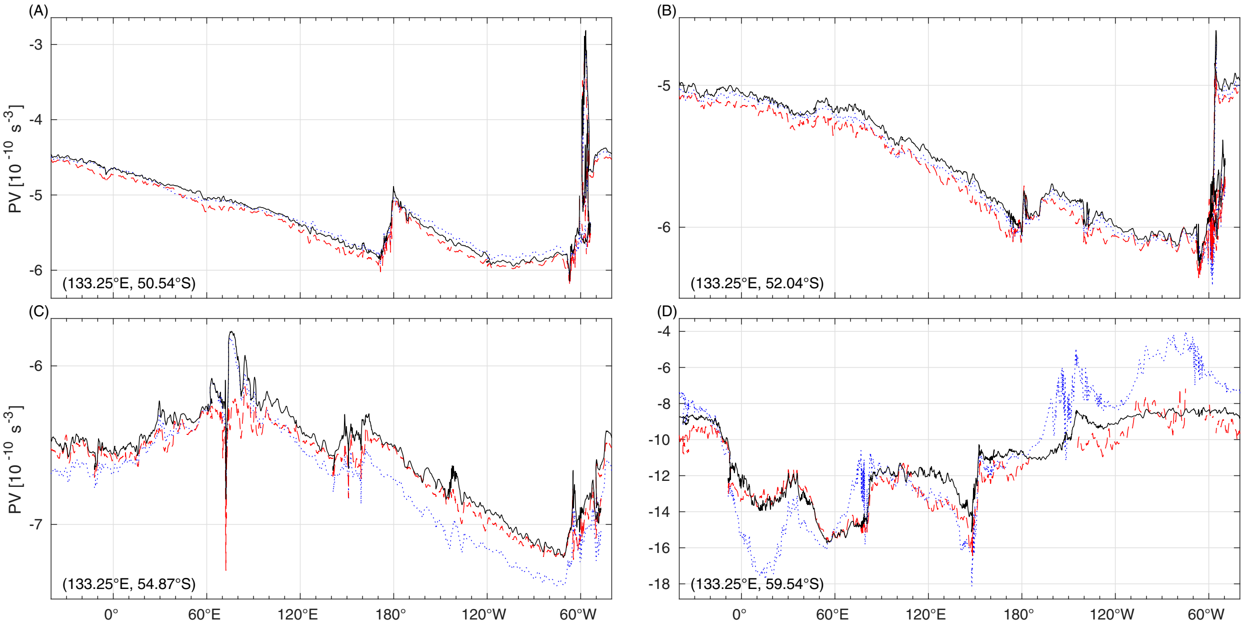

FIG. B1. Comparison of different definitions for PV along geostrophic streamlines: the Ertel–Euler PV $Q^\#$ from (35) on Montgomery streamlines on $\overline{b} = b_0$ (solid black); the TWA PV $\Pi^\#$ from (B4) on Montgomery streamlines on the surface $b = b_0$ (dashed red); the Euler–Ertel PV $\overline{Q^{\sigma_1}}$ from (B1) on orthobaric Montgomery streamlines on a σ_1 surface (dotted blue). The $\overline{b}$ and σ_1 surfaces intersect (133.25°E, 54.04°S) at -700 m, while the mean height of the b surface is very near -700 m here. The streamlines cross 133.25°E at the indicated latitudes, as in Fig. 2.

tracer grid. This gives a 5-day mean Q^{σ_1}, the arithmetic mean of which gives $\overline{Q^{\sigma_1}}$. We linearly interpolate $\overline{Q^{\sigma_1}}$ vertically onto the isosurface $\overline{\sigma_1} = 32.090761$ kg m^{-3} (Gille used 32.3 kg m^{-3}), which intersects the reference point (x_0, y_0, z_0) = (133.25°E, 54.0416°S, -700 m). Finally, we linearly interpolate $\overline{Q^{\sigma_1}}$ on the surface horizontally onto a geostrophic streamline, as before.

b. Thickness-weighted average PV

1) DEFINITION

The TWA formalism (Young 2012) uses a new coordinate system, $(\tilde{x},\tilde{y},\tilde{b},\tilde{t})$, related to Cartesian (x, y, z, t) by $\tilde{x} = x$, $\tilde{y} = y$, $\tilde{b} = b(x,y,z,t)$, and $\tilde{t} = t$. Under TWA, buoyancy $\tilde{b}$ is an independent variable, while height ξ is a dependent variable. The layer thickness is

$$h = \xi_{\tilde{b}}. \tag{B2}$$

The thickness-weighted average of any scalar field F is

$$\widehat{F} = \overline{Fh}/\overline{h}. \tag{B3}$$

The time-mean is taken at constant buoyancy, since F and h are functions of $(\tilde{x},\tilde{y},\tilde{b},\tilde{t})$. The TWA PV is

$$\Pi^\# = \frac{f + \widehat{v}_{\tilde{x}} - \widehat{u}_{\tilde{y}}}{\overline{h}}. \tag{B4}$$

Note the TWA does not commute with partial derivatives: $(\widehat{F})_{\tilde{x}} \neq \widehat{(F_{\tilde{x}})}$. The notation $\widehat{F}_{\tilde{x}}$ is shorthand for $(\widehat{F})_{\tilde{x}}$ (TWA first, derivative second).

2) GEOSTROPHIC STREAMFUNCTION

The Montgomery potential (23) is appropriately modified by Laisant's inverse integral rule:

$$m(\tilde{x},\tilde{y},\tilde{b},\tilde{t}) = \frac{1}{\rho_c} p_1(\tilde{x},\tilde{y},\tilde{t}) - b_1(\tilde{x},\tilde{y},\tilde{t})\, z_1 + \int_{\tilde{b}}^{b_1(\tilde{x},\tilde{y},\tilde{t})} \xi(\tilde{x},\tilde{y},\tilde{b}',\tilde{t})\, d\tilde{b}', \tag{B5}$$

where $b_1(\tilde{x},\tilde{y},\tilde{t}) = b(x,y,z_1,t)$ is the buoyancy at height z_1—implicitly defined by $\xi(\tilde{x},\tilde{y},b_1(\tilde{x},\tilde{y},\tilde{t}),\tilde{t}) = z_1$.

3) NUMERICS

To calculate $\Pi^\#$, we use piecewise cubic Hermite interpolating polynomials (PCHIPs) because they preserve monotonicity and are continuously differentiable at knots. Specifically, $\xi(\tilde{x},\tilde{y},\tilde{b},\tilde{t})$ is obtained as the PCHIP for z as a function of b at each $(\tilde{x},\tilde{y},\tilde{t})$. Then, the layer thickness $h = \xi_{\tilde{b}}$ is obtained by analytic differentiation. Similarly, we use PCHIPs to vertically interpolate u, averaged onto the tracer grid, onto $b = b_0$, and similarly for v. We repeat this for each 5-day average to assemble $\overline{h}, \widehat{u}$ and $\widehat{v}$ via (B3). The time-mean Montgomery potential $\overline{m}$ is assembled from each 5-day m, themselves obtained from (B5) with the integral evaluated analytically.

For reference, the time-mean height of the $b = b_0$ surface at (x_0, y_0) = (133.25°E, 54.0416°S) is $\overline{\xi(x_0,y_0,b_0,t)} = -698.3$ m. This differs from the height of the time-mean buoyancy surface $\overline{b} = b_0$, which is $\xi^\#(x_0,y_0,b_0) = z_0 = -700.0$ m. This difference (of 1.7 m) is important for self-consistency in the TWA framework (Young 2012), and is the essential difference between McDougall and McIntosh (1996) and McDougall and McIntosh (2001).

c. Relation between three time-mean PVs

The Ertel–Euler PV $Q^\#$ somewhat resembles the TWA PV $\Pi^\#$, at least more so than does the Euler–Ertel PV. Consider the thin-film limit, which neglects horizontal contributions to the PV:

$$Q^\# \approx (f + \overline{\zeta})\overline{b_z} = \overline{(f + \zeta)b_z h}\,\overline{h^{-1}}, \tag{B6}$$

using (B2). Hence, $Q^\#$ resembles the TWA of the thin-film PV $(f + \zeta)b_z$, albeit with two differences. First, $\Pi^\#$ involves division by $\overline{h} = \overline{b_z^{-1}}$, which is equivalent to multiplication by the harmonic time-mean of b_z, but (B6) involves multiplication by the arithmetic time-mean of $b_z = h^{-1}$. Second and more importantly, for $Q^\#$ the time-mean is Eulerian, sampling from a constant depth, whereas for $\Pi^\#$ the time-mean is quasi-Lagrangian, sampling from a buoyancy surface as it heaves vertically.

d. Results

Figure B1 verifies that $Q^\#$, $\Pi^\#$, and $\overline{Q^{\sigma_1}}$ show qualitatively similar structure along streamlines in the Southern Ocean. The most notable outlier is $\overline{Q^{\sigma_1}}$ on the most southerly streamlines, likely caused by significant differences in the depth of σ_1 and $\tilde{b}$ surfaces where these rise toward the sea surface.

APPENDIX C

Thickness-Weighted Average Momentum, Thickness, and PV Budgets

Here, we review the necessary TWA theory to reach the PV budget (for full details, see Young 2012) interspersed with our numerical methods. Then, we illuminate and quantify the numerical problems of using TWA with archived z-level model diagnostics.

a. Theory and methods

1) COORDINATE-TRANSFORMATIONS AND AVERAGES

Further to the TWA background provided in appendix B, transforming between z coordinates and buoyancy coordinates employs the following transformations of the partial derivatives:

$$(\cdot)_{\tilde{x}} = (\cdot)_x + \xi_{\tilde{x}}\,(\cdot)_z, \tag{C1a}$$

$$(\cdot)_{\tilde{y}} = (\cdot)_y + \xi_{\tilde{y}}(\cdot)_z, \tag{C1b}$$

$$(\cdot)_{\tilde{b}} = \xi_{\tilde{b}}(\cdot)_z, \tag{C1c}$$

$$(\cdot)_{\tilde{t}} = (\cdot)_t + \xi_{\tilde{t}}\,(\cdot)_z. \tag{C1d}$$

Applying (C1) to the buoyancy $\tilde{b}$ reveals

$$\xi_{\tilde{x}} = -b_x h, \tag{C2a}$$

$$\xi_{\tilde{y}} = -b_y h, \tag{C2b}$$

$$h = \xi_{\tilde{b}} = b_z^{-1}, \tag{C2c}$$

$$\xi_{\tilde{t}} = -b_t h. \tag{C2d}$$

Two types of Reynolds decompositions are needed: fluctuations from the average,

$$\alpha' \equiv \alpha - \overline{\alpha}, \tag{C3}$$

and fluctuations from the thickness-weighted average,

$$\alpha'' \equiv \alpha - \widehat{\alpha}. \tag{C4}$$

2) INTERPOLATION

We evaluate ξ, $h = \xi_{\tilde{b}}$, u, υ, and m using PCHIPs [appendix B, section b(3)], but evaluate terms in the z-level buoyancy and momentum equations on a buoyancy surface using linear interpolation. Linear interpolants, unlike PCHIPs, preserve equations: terms that sum to zero on a grid also sum to zero after each term is linearly interpolated between grid points. (Cubic spline interpolation also preserves equations, but can overshoot the data—particularly problematic near the pycnocline.)

3) BUOYANCY-COORDINATE THICKNESS EQUATION

To derive the thickness equation, apply the manipulation $\mathscr{F}[\cdot] = -h\partial_z(h\cdot)$ to the Cartesian buoyancy Eq. (29) using (C1) and (C2). Term by term, this gives

$$\mathscr{F}[b_t] \qquad\qquad = h_{\tilde{t}}, \tag{C5a}$$

$$\mathscr{F}[ub_x] + hu_x = (hu)_{\tilde{x}}, \tag{C5b}$$

$$\mathscr{F}[\upsilon b_y] + h\upsilon_y = (h\upsilon)\tilde{y}, \tag{C5c}$$

$$\mathscr{F}[wb_z] + hw_z = 0, \tag{C5d}$$

$$-\mathscr{F}[\varpi] \qquad\qquad = (h\varpi)_{\tilde{b}}. \tag{C5e}$$

For (C5d), it was crucial that $h = b_z^{-1}$ so that w stands alone before taking the z derivative. This enables continuity, (33), to annihilate the second column of (C5), while the first column sums to zero by (29) and linearity of $\mathscr{F}$. Thus, the RHS sums to zero, providing the buoyancy-coordinate thickness equation:

$$h_{\tilde{t}} + (hu)_{\tilde{x}} + (h\upsilon)_{\tilde{y}} + (h\varpi)_{\tilde{b}} = 0. \tag{C6}$$

Numerically, we implement $\mathscr{F}$ as follows. Average the input from the tracer grid onto the W grid, then divide by

b_z calculated by first difference. Take the z derivative by first difference, returning to the tracer grid. Linearly interpolate this onto the buoyancy surface. Multiply by $-h = -\xi_{\tilde b}$. We found this approach best among many numerical implementations of $\mathscr{F}$ that we tested, trying to minimize the thickness error (see appendix C, section b).

4) TWA THICKNESS EQUATION

Noting that $\overline{h}\widehat{u} = \overline{hu}$, $\overline{h}\widehat{v} = \overline{hv}$, and $\overline{h}\widehat{\varpi} = \overline{h\varpi}$, the time-mean of (C6) immediately yields the TWA thickness equation,

$$\overline{h}_{\tilde t} + (\widehat{u}\overline{h})_{\tilde x} + (\widehat{v}\overline{h})_{\tilde y} + (\widehat{\varpi}\overline{h})_{\tilde b} = 0. \tag{C7}$$

This has no eddy terms; they are confined to the momentum equation, shown next. Numerically, we form (C7) simply by averaging (C6).

5) BUOYANCY COORDINATE MOMENTUM EQUATION

The zonal component of the (Boussinesq, hydrostatic, traditional) z-coordinate momentum Eq. (24) transforms term by term into buoyancy coordinates as

$$u_{\tilde t} = u_t - hb_t u_z, \tag{C8a}$$

$$\varpi u_{\tilde b} = wu_z + hb_t u_z + hb_x uu_z + hb_y vu_z, \tag{C8b}$$

$$-(f + v_{\tilde x} - u_{\tilde y})v = -(f + v_x - u_y)v + hb_x vv_z - hb_y vu_z, \tag{C8c}$$

$$K_{\tilde x} = K_x - hb_x vv_z - hb_x uu_z, \tag{C8d}$$

$$m_{\tilde x} = \Phi_x, \tag{C8e}$$

$$-F^{(X)} = -F^{(X)}. \tag{C8f}$$

The first column on the RHS provides (24), obtained from SOSE's 5-day diagnostics. The other RHS columns sum to zero. Hence, the LHS provides the zonal momentum equation in buoyancy coordinates:

$$u_{\tilde t} + \varpi u_{\tilde b} - v(f + v_{\tilde x} - u_{\tilde y}) + m_{\tilde x} + K_{\tilde x} = F^{(X)}. \tag{C9}$$

Note (C8e) and its meridional version $m_{\tilde y} = \Phi_y$ together are only valid because our b surfaces possess an exact geostrophic streamfunction, m (section 3a). Numerically, the first column of the RHS of (C8) is obtained by interpolation of model outputs onto ξ averaged onto the u grid, while other RHS terms are calculated directly on the buoyancy surface with averages onto the u grid as necessary, and hb_x and hb_y taken as $-\xi_{\tilde x}$ and $-\xi_{\tilde y}$, respectively. The meridional momentum equation is treated similarly.

6) TWA MOMENTUM EQUATION

Considering that $\widehat{u} = \overline{hu}/\overline{h}$, multiply (C9) by h, time average, then divide by $\overline{h}$. Prior to the last step, this yields

$$\overline{h}\widehat{u}_{\tilde t} = \overline{hu_{\tilde t}} - \overline{h}_{\tilde t}\widehat{u} + \overline{h_{\tilde t}u}, \tag{C10a}$$

$$\overline{h}\widehat{\varpi}\widehat{u}_{\tilde b} + (\overline{h}\widehat{\varpi''u''})_{\tilde b} = \overline{h\varpi u_{\tilde b}} - (\overline{h}\widehat{\varpi})_{\tilde b}\widehat{u} + \overline{(h\varpi)_{\tilde b}u}, \tag{C10b}$$

$$-\overline{h}(f + \widehat{v}_{\tilde x} - \widehat{u}_{\tilde y})\widehat{v} + (\overline{h}\widehat{v''u''})_{\tilde y} = -\overline{h(f + v_{\tilde x} - u_{\tilde y})v} - (\overline{h}\widehat{v})_{\tilde y}\widehat{u} + \overline{(hv)_{\tilde y}u} + C, \tag{C10c}$$

$$\overline{h}\,\frac{1}{2}(\widehat{u}^2 + \widehat{v}^2)_{\tilde x} + (\overline{h}\widehat{u''u''})_{\tilde x} = \overline{hK_{\tilde x}} - (\overline{h}\widehat{u})_{\tilde x}\widehat{u} + \overline{(hu)_{\tilde x}u} - C, \tag{C10d}$$

$$\overline{h}\,\overline{m}_{\tilde x} + \overline{h'm'_{\tilde x}} = \overline{hm_{\tilde x}}, \tag{C10e}$$

$$-\overline{h}\widehat{F^{(X)}} = -\overline{hF^{(X)}}, \tag{C10f}$$

where

$$C = (\overline{h}\widehat{v})_{\tilde x}\widehat{v} + (\overline{h}\widehat{v''v''})_{\tilde x} - \overline{(hv)_{\tilde x}v}. \tag{C11}$$

Each column on the RHS of (C10) sums to zero: the first column is the time-mean of h times (C9); the second column is $\widehat{u}$ times (C7); the third column is the time-mean of u times (C6).

Hence, dividing (C10) by $\overline{h}$ provides the buoyancy-coordinate TWA zonal momentum equation,

$$\widehat{u}_{\tilde{t}} + \widehat{\varpi}\widehat{u}_{\tilde{b}} - (f + \widehat{v}_{\tilde{x}} - \widehat{u}_{\tilde{y}})\widehat{v} + \left(\overline{m} + \frac{1}{2}\widehat{u}^2 + \frac{1}{2}\widehat{v}^2\right)_{\tilde{x}} = \widehat{F^{(X)}} - E^u, \tag{C12}$$

where

$$E^u = \underbrace{\overline{h}^{-1}\left[(\overline{h}\widehat{u''u''})_{\tilde{x}} + (\overline{h}\widehat{v''u''})_{\tilde{y}} + \left(\frac{1}{2}\overline{\xi'2}\right)_{\tilde{x}}\right]}_{E^u_{\text{Reynolds/Iso}}} + \underbrace{\overline{h}^{-1}(\overline{h}\widehat{\varpi''u''})_{\tilde{b}}}_{E^u_{\text{Reynolds/Dia}}} + \underbrace{\overline{h}^{-1}(\overline{\xi' m'_{\tilde{x}}})_{\tilde{b}}}_{E^u_{\text{EFS}}} \tag{C13}$$

collects the eddy-forcing terms. The first four terms in E^u are Reynolds stresses, while the last is the eddy form stress, which derives from and dominates the RHS of

$$\overline{h' m'_{\tilde{x}}} = \left(\frac{1}{2}\overline{\xi'^2}\right)_{\tilde{x}} + (\overline{\xi' m'_{\tilde{x}}})_{\tilde{b}}. \tag{C14}$$

The first three (last two) terms in E^u transport momentum within (across) buoyancy surfaces.

Numerically, the Reynolds terms in the second column of (C10) are taken as residuals, with all other terms directly computed. The vorticity and kinetic energy terms (C10c) and (C10d) are added, so C is not computed and $(hu)_{\tilde{x}} + (hv)_{\tilde{y}}$ is not split, instead taken together as $\overline{\mathscr{F}[\mathbf{v}\cdot\nabla b]}$. The eddy form stress is obtained from (C14), with $\overline{h' m'_{\tilde{x}}}$ the residual of (C10e).

For (C10b) we require $\widehat{u}_{\tilde{b}}$. We might expand $\widehat{u}_{\tilde{b}} = \overline{h}^{-1}(\overline{h_{\tilde{b}} u} + \overline{h u_{\tilde{b}}} - \overline{h_{\tilde{b}}}\widehat{u})$, but this requires $h_{\tilde{b}} = \xi_{\tilde{b}\tilde{b}}$, which is discontinuous for C1 interpolants like PCHIPs. Instead, we compute $\widehat{u}$ on a second, nearby buoyancy surface and take a finite difference.

The meridional TWA momentum budget is derived and handled similarly, yielding

$$\widehat{v}_{\tilde{t}} + \widehat{\varpi}\widehat{v}_{\tilde{b}} + (f + \widehat{v}_{\tilde{x}} - \widehat{u}_{\tilde{y}})\widehat{u} + \left(\overline{m} + \frac{1}{2}\widehat{u}^2 + \frac{1}{2}\widehat{v}^2\right)_{\tilde{y}} = \widehat{F^{(Y)}} - E^v, \tag{C15}$$

where

$$E^v = \underbrace{\overline{h}^{-1}\left[(\overline{h}\widehat{u''v''})_{\tilde{x}} + (\overline{h}\widehat{v''v''})_{\tilde{y}} + \left(\frac{1}{2}\overline{\xi'2}\right)_{\tilde{y}}\right]}_{E^v_{\text{Reynolds/Iso}}} + \underbrace{\overline{h}^{-1}(\overline{h}\widehat{\varpi''v''})_{\tilde{b}}}_{E^v_{\text{Reynolds/Dia}}} + \underbrace{\overline{h}^{-1}(\overline{\xi' m'_{\tilde{y}}})_{\tilde{b}}}_{E^v_{\text{EFS}}}. \tag{C16}$$

7) TWA POTENTIAL VORTICITY EQUATION

Cross differentiating the TWA momentum Eqs. (C12) and (C15) yields the TWA vorticity equation,

$$(\overline{h}\Pi^{\#})_{\tilde{t}} + \left(\widehat{\varpi}\widehat{v}_{\tilde{b}} + \overline{h}\widehat{u}\Pi^{\#}_{\tilde{x}}\right) - (\widehat{\varpi}\widehat{u}_{\tilde{b}} - \overline{h}\widehat{v}\Pi^{\#})_{\tilde{y}} = \left(\widehat{F^{(Y)}} - E^v\right)_{\tilde{x}} - \left(\widehat{F^{(X)}} - E^u\right)_{\tilde{y}}. \tag{C17}$$

The value of PV lies in canceling the vortex stretching term $\overline{h}\Pi^{\#}(\widehat{u}_{\tilde{x}} + \widehat{v}_{\tilde{y}})$ latent in (C17) with the thickness stretching term $\overline{h}(\widehat{u}_{\tilde{x}} + \widehat{v}_{\tilde{y}})$ latent in (C7). Thus, (C17) $-\Pi^{\#}$(C7)$/\overline{h}$ yields the TWA PV equation,

$$\underbrace{\Pi^{\#}_{\tilde{t}}}_{\text{tendency}} + \underbrace{\widehat{u}\Pi^{\#}_{\tilde{x}} + \widehat{v}\Pi^{\#}_{\tilde{y}}}_{\text{isopycnal advection}} + \underbrace{\widehat{\varpi}\Pi^{\#}_{\tilde{b}}}_{\text{diapycnal advection}} = \underbrace{\overline{h}^{-1}\left(\widehat{F^{(Y)}}_{\tilde{x}} - \widehat{F^{(X)}}_{\tilde{y}}\right)}_{\text{mechanical forcing}} - \underbrace{\overline{h}^{-1}\left(E^v_{\tilde{x}} - E^u_{\tilde{y}}\right)}_{\text{eddy forcing}} + \underbrace{\overline{h}^{-1}\left[(\overline{h}\widehat{\varpi}\Pi^{\#})_{\tilde{b}} - (\widehat{\varpi}\widehat{v}_{\tilde{b}})_{\tilde{x}} + (\widehat{\varpi}\widehat{u}_{\tilde{b}})_{\tilde{y}}\right]}_{\text{diapycnal shear}}. \tag{C18}$$

The LHS is the material derivative of $\Pi^{\#}$ following the TWA velocity. Hence, $\Pi^{\#}$ is materially conserved, except for the effects of mechanical forcing and dissipation, eddies, and nonconservation of buoyancy.

b. Numerical errors

Numerical discretization of the TWA PV budget (C18) suffers predominantly from two numerical errors: a thickness error and a stretching error. These errors ultimately infect the in-buoyancy-surface PV advection, which is, theoretically,

$$\widehat{u}\Pi^{\#}_{\tilde{x}} + \widehat{v}\Pi^{\#}_{\tilde{y}} = \frac{\widehat{u}(f + \widehat{v}_{\tilde{x}} - \widehat{u}_{\tilde{y}})_{\tilde{x}} + \widehat{v}(f + \widehat{v}_{\tilde{x}} - \widehat{u}_{\tilde{y}})_{\tilde{y}}}{\overline{h}} - \frac{\Pi^{\#}}{\overline{h}}(\widehat{u}\overline{h}_{\tilde{x}} + \widehat{v}\overline{h}_{\tilde{y}}). \tag{C19}$$

On the RHS, we can add and subtract the stretching term $\Pi^{\#}(\widehat{u}_{\tilde{x}} + \widehat{v}_{\tilde{y}})$. The added term combines with the vorticity advection to produce $\overline{h}^{-1}$ times $(\overline{h}\widehat{u}\Pi^{\#})_{\tilde{x}} + (\overline{h}\widehat{v}\Pi^{\#})_{\tilde{y}}$, which appears in the TWA vorticity budget (C17). The subtracted term combines with the thickness advection to produce $\Pi^{\#}/\overline{h}$ times $(\widehat{u}\overline{h})_{\tilde{x}} + (\widehat{v}\overline{h})_{\tilde{y}}$, which appears in the TWA thickness budget (C7). The stretching error arises because thickness and vorticity live on different parts of the numerical C-grid, so their stretching terms do not cancel. The thickness error arises because the z-level buoyancy and continuity equations are both delicately balanced and cannot be transformed into the TWA thickness term $(\widehat{u}\overline{h})_{\tilde{x}} + (\widehat{v}\overline{h})_{\tilde{y}}$ with $\overline{h}$, $\widehat{u}$, and $\widehat{v}$ evaluated on the buoyancy surface, as is required for consistency with the TWA vorticity equation.

Some notation will help understand this in greater detail. Let a coordinate-decorated overbar denote an average of neighboring data points onto a different grid. For example, $\overline{b}^x$ averages b onto the u grid, and $\overline{u}^{xy}$ averages u onto the v grid. Any two variables α and β on the same grid satisfy

$$(\alpha\beta)_z = \alpha_z\overline{\beta}^z + \overline{\alpha}^z\beta_z, \tag{C20}$$

regardless of grid spacing, or whether the discretized derivatives use forward, backward, or centered differences. Clearly, (C20) also holds for other partial derivatives.

Starting with the thickness error, note that the buoyancy equation (29) is discretized on a C-grid as[5]

$$b_t + (u\overline{b}^{x})_x + (v\overline{b}^{y})_y + (w\overline{b}^{z})_z = \varpi. \tag{C21}$$

Using (C20), this is

$$b_t + u_x\overline{b}^{xx} + \overline{u}^{x}\overline{b}^{x}_{x} + v_y\overline{b}^{yy} + \overline{v}^{y}\overline{b}^{y}_{y} + w_z\overline{b}^{zz} + \overline{w}^{z}\overline{b}^{z}_{z} = \varpi\cdot \tag{C22}$$

Applying $\mathscr{F}$ to (C22) first divides by b_z, which does not isolate w for the continuity equation to annihilate, as needed in (C5). Thus, $\mathscr{F}[\mathbf{v}\cdot\nabla b]$ cannot equal $(hu)_{\tilde{x}} + (hv)_{\tilde{y}}$ numerically with the latter calculated using u, v, and h on the buoyancy surface. This numerical imbalance is severe, because the buoyancy and continuity equations are both extremely finely balanced.

To understand the stretching error, first suppose we form $\Pi^\#$ on the tracer grid: $\Pi^\# = \overline{(f + \widehat{v}_{\tilde{x}} - \widehat{u}_{\tilde{y}})}^{xy}/\overline{h}$. Discretizing (C19) on the C-grid with a second-order centered advection scheme for each of the PV, vorticity, and thickness advection terms yields

$$\left(\widehat{u}\overline{\Pi^\#}^{x}\right)_{\tilde{x}} + \left(\widehat{v}\overline{\Pi^\#}^{y}\right)_{\tilde{y}} - \Pi^\#(\widehat{u}_{\tilde{x}} + \widehat{v}_{\tilde{y}}) = \frac{1}{\overline{h}}\left[\overline{\left[\overline{(f + \widehat{v}_{\tilde{x}} - \widehat{u}_{\tilde{y}})}^{x}\,\overline{\overline{\widehat{u}}}^{xy}\right]_{\tilde{x}} + \left[\overline{(f + \widehat{v}_{\tilde{x}} - \widehat{u}_{\tilde{y}})}^{y}\,\overline{\overline{\widehat{v}}}^{xy}\right]_{\tilde{y}}}^{xy} - \overline{(f + \widehat{v}_{\tilde{x}} - \widehat{u}_{\tilde{y}})\left(\overline{\overline{\widehat{u}}}^{xy}_{\tilde{x}} + \overline{\overline{\widehat{v}}}^{xy}_{\tilde{y}}\right)}^{xy}\right]$$
$$- \frac{\Pi^\#}{\overline{h}}\left\{\left[\left(\widehat{u}\overline{\overline{h}}^{x}\right)_{\tilde{x}} + \left(\widehat{v}\overline{\overline{h}}^{y}\right)_{\tilde{y}}\right] - \overline{h}(\widehat{u}_{\tilde{x}} + \widehat{v}_{\tilde{y}})\right\} + \epsilon^{(\mathrm{Advec})}. \tag{C23}$$

On the RHS, vorticity is advected by $\widehat{u}$ and $\widehat{v}$ averaged onto the v and u grids, correctly producing terms in the discretized version of (C17). The LHS, however, contains vorticity averaged onto the tracer grid being advected by $\widehat{u}$ and $\widehat{v}$ on the u and v grids. This difference is captured by $\epsilon^{(\mathrm{Advec})}$, taken as a residual. Provided the model resolution is such that the horizontal velocity varies smoothly laterally, this advection error is small relative to other terms (Fig. C1).

The stretching and thickness errors are exposed by rearranging (C23) as

$$\left(\widehat{u}\overline{\Pi^\#}^{x}\right)_{\tilde{x}} + \left(\widehat{v}\overline{\Pi^\#}^{y}\right)_{\tilde{y}} - \Pi^\#(\widehat{u}_{\tilde{x}} + \widehat{v}_{\tilde{y}}) = \epsilon^{(\mathrm{Stretch})} + \epsilon^{(\mathrm{Thick})}$$
$$+ \epsilon^{(\mathrm{Advec})} + \frac{1}{\overline{h}}\overline{\left[\overline{(f + \widehat{v}_{\tilde{x}} - \widehat{u}_{\tilde{y}})}^{x}\,\overline{\overline{\widehat{u}}}^{xy}\right]_{\tilde{x}} + \left[\overline{(f + \widehat{v}_{\tilde{x}} - \widehat{u}_{\tilde{y}})}^{y}\,\overline{\overline{\widehat{v}}}^{xy}\right]_{\tilde{y}}}^{xy}$$
$$- \frac{\Pi^\#}{\overline{h}}\overline{\mathscr{F}[\mathbf{v}\cdot\nabla b]}, \tag{C24}$$

where

$$\epsilon^{(\mathrm{Stretch})} = \Pi^\#(\widehat{u}_{\tilde{x}} + \widehat{v}_{\tilde{y}}) - \frac{1}{\overline{h}}\overline{(f + \widehat{v}_{\tilde{x}} - \widehat{u}_{\tilde{y}})\left(\overline{\overline{\widehat{u}}}^{xy}_{\tilde{x}} + \overline{\overline{\widehat{v}}}^{xy}_{\tilde{y}}\right)}^{xy} \tag{C25}$$

captures the numerical imbalance between the stretching terms, and

$$\epsilon^{(\mathrm{Thick})} = \frac{\Pi^\#}{\overline{h}}\left[\overline{\mathscr{F}[\mathbf{v}\cdot\nabla b]} - \left(\widehat{u}\overline{\overline{h}}^{x}\right)_{\tilde{x}} - \left(\widehat{v}\overline{\overline{h}}^{y}\right)_{\tilde{y}}\right] \tag{C26}$$

captures the thickness equation's numerical imbalance. The non-ϵ terms on the RHS of (C24) are (rescaled) terms in the TWA vorticity equation (C17) and in the version of the TWA thickness equation (C7) that can be numerically balanced, i.e., $\overline{\mathscr{F}[(29)]}$.

c. Results: TWA PV budget in the Southern Ocean

Figure C1 maps terms in the TWA PV budget (C18), with the in-buoyancy-surface advective terms calculated from the LHS of (C24), but further separated into rotational and divergent components found by a Helmholtz decomposition of $(\widehat{u}, \widehat{v})$. Despite the quasi-Lagrangian averaging, PV tendency remains large, caused by significant drift of layer thickness throughout SOSE's record. Reynolds stresses within the buoyancy surface are surprisingly significant, but eddy form stress is dominant, as expected. Unfortunately, the thickness error $\epsilon^{(\mathrm{Thick})}$ is among the largest terms in the PV budget, and the stretching error $\epsilon^{(\mathrm{Stretch})}$ is also sizeable (and substantially worse without smoothing—not shown).

To study the source of the thickness error, we repeat the PV budget with an alternate prescription of the thickness advection and stretching term, $(\widehat{u}\overline{h})_{\tilde{x}} + (\widehat{v}\overline{h})_{\tilde{y}}$. Before, this was computed as $\overline{\mathscr{F}[\mathbf{v}\cdot\nabla b]}$ with $\mathbf{v}\cdot\nabla b$ obtained from (30b) using model diagnostics for salt and heat fluxes. Now, we continue using $\overline{\mathscr{F}[\mathbf{v}\cdot\nabla b]}$, but calculate $\mathbf{v}\cdot\nabla b$ using SOSE's third-order upwind advection scheme with $\mathbf{v}$ the 5-day Eulerian-averaged velocity field and $b = R(S, \theta, -g\rho_c z)$ the buoyancy field calculated from the 5-day Eulerian-averaged S and θ. This means the 5-day buoyancy budget (29) will not close, hence the buoyancy forcing is now taken as the residual, $\varpi \equiv b_t + \mathbf{v}\cdot\nabla b$. Having marred the fine balance between large terms in the buoyancy equation, this new ϖ is over an order of magnitude larger than the true ϖ, and this will appear as fictitious diapycnal forcing in the PV budget. The goal here is not to fix the PV budget, but merely to locate the source of $\epsilon^{(\mathrm{Thick})}$.

Figure C2 shows the PV budget under this alternative prescription. The thickness error is considerably reduced compared to Fig. C1, suggesting our numerical treatment of the coordinate transformation works decently (though still

---

[5] This second-order centered advection scheme for buoyancy is simpler than SOSE's third-order upwind advection scheme for salinity and potential temperature, but is sufficient to illustrate the grid problems.

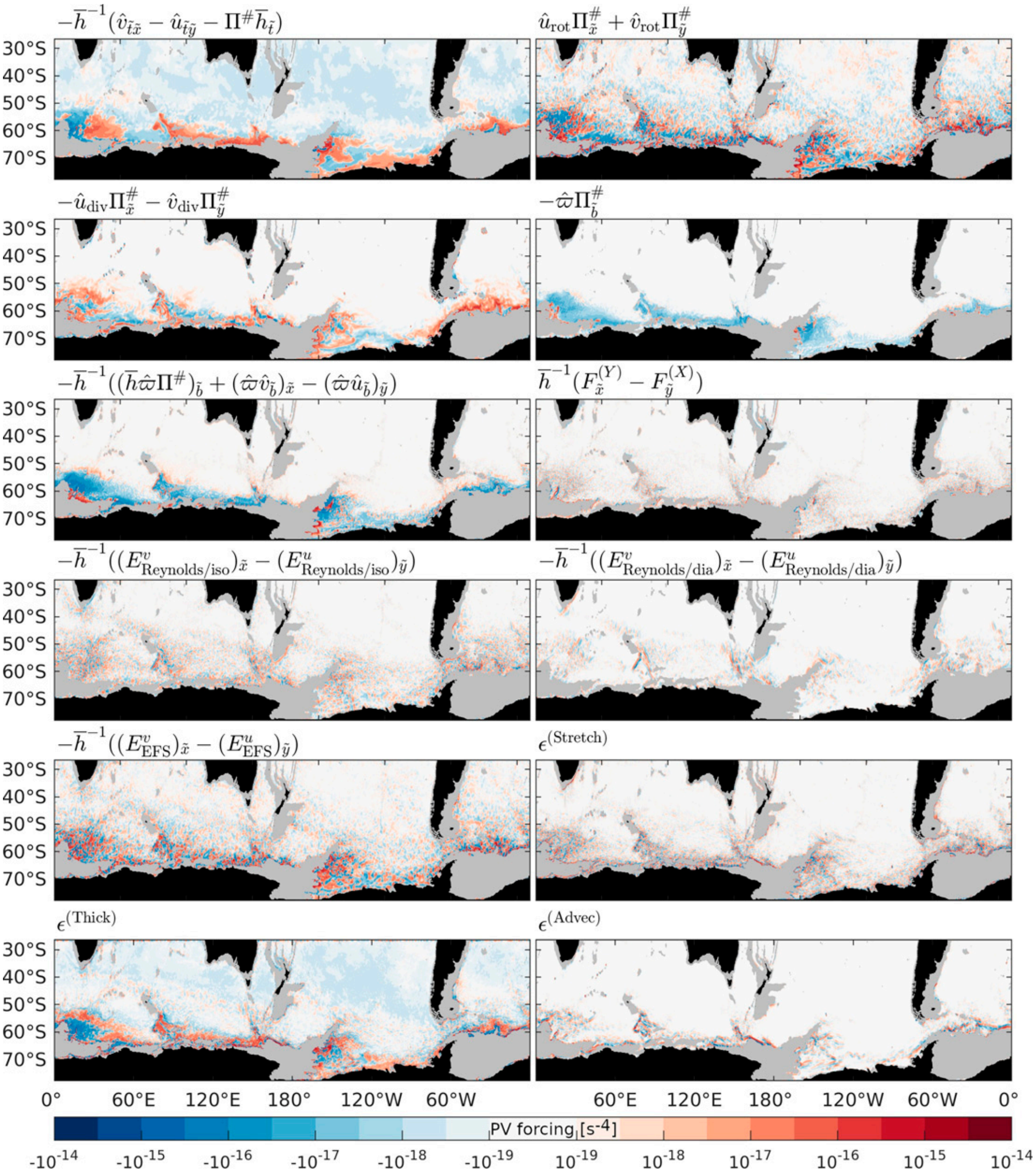

$-\overline{h}^{-1}(\hat{v}_{\tilde{t}\tilde{x}} - \hat{u}_{\tilde{t}\tilde{y}} - \Pi^{\#}\overline{h}_{\tilde{t}})$

$\hat{u}_{\mathrm{rot}}\Pi^{\#}_{\tilde{x}} + \hat{v}_{\mathrm{rot}}\Pi^{\#}_{\tilde{y}}$

$-\hat{u}_{\mathrm{div}}\Pi^{\#}_{\tilde{x}} - \hat{v}_{\mathrm{div}}\Pi^{\#}_{\tilde{y}}$

$-\hat{\varpi}\Pi^{\#}_{\tilde{b}}$

$-\overline{h}^{-1}((\overline{h}\hat{\varpi}\Pi^{\#})_{\tilde{b}} + (\hat{\varpi}\hat{v}_{\tilde{b}})_{\tilde{x}} - (\hat{\varpi}\hat{u}_{\tilde{b}})_{\tilde{y}})$

$\overline{h}^{-1}(F^{(Y)}_{\tilde{x}} - F^{(X)}_{\tilde{y}})$

$-\overline{h}^{-1}((E^{v}_{\mathrm{Reynolds/iso}})_{\tilde{x}} - (E^{u}_{\mathrm{Reynolds/iso}})_{\tilde{y}})$

$-\overline{h}^{-1}((E^{v}_{\mathrm{Reynolds/dia}})_{\tilde{x}} - (E^{u}_{\mathrm{Reynolds/dia}})_{\tilde{y}})$

$-\overline{h}^{-1}((E^{v}_{\mathrm{EFS}})_{\tilde{x}} - (E^{u}_{\mathrm{EFS}})_{\tilde{y}})$

$\epsilon^{(\mathrm{Stretch})}$

$\epsilon^{(\mathrm{Thick})}$

$\epsilon^{(\mathrm{Advec})}$

FIG. C1. Maps of thickness-weighted average potential vorticity forcing terms (s^{-4}) on the buoyancy surface $b = b$ (133.25°E, 54.04°S, −1000 m, 18–22 Sep 2008). From left to right and then from top to bottom, panels show tendency, rotational advection, divergent advection, diapycnal advection, diapycnal shear, momentum forcing, isopycnal Reynolds stresses, diapycnal Reynolds stresses, eddy form stress, stretching error, thickness error, and advection error. All maps are smoothed with a Gaussian filter of 5 × 5 grid points, and masked out (light gray) where the surface incropped or outcropped at any time during the record.

not perfectly). However, the errors are shunted to diapycnal forcings: predominantly the diapycnal shear, with smaller adjustments to the diapycnal advection and diapycnal Reynolds stress. This implies that a proper TWA analysis of PV cannot be done with SOSE's Eulerian 5-day averaged data.

Higher-frequency output is required, but most likely TWA should be done online. Indeed, Uchida et al. (2021) "found the difference between the eddy–eddy correlation terms diagnosed from instantaneous and temporally averaged fields to be up to same order of the total variance of the instantaneous field." The buoyancy surface used in Figs. C1 and C2 can change by 200 m from one 5-day window to the next, in SOSE's ACC. Even if TWA is done online, though, the not-insignificant stretching and advective errors would remain.

d. Discussion

Some recent studies have used the TWA formalism to study ocean dynamics using z-level models (Cessi and Wolfe 2013; Aoki et al. 2016), without simultaneously and

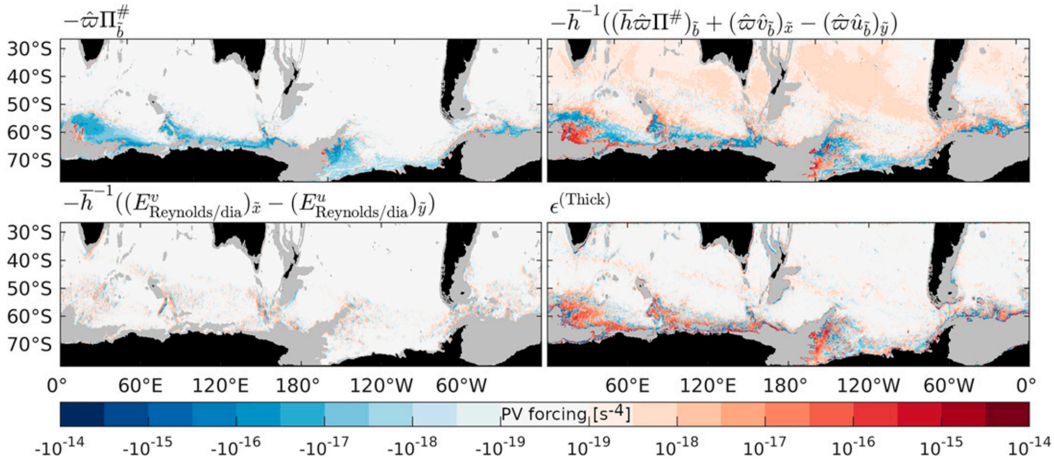

FIG. C2. As in Fig. C1, but having instead computed the z-coordinate buoyancy advection offline, using the 5-day Eulerian-mean velocity and buoyancy computed from the 5-day Eulerian mean salinity and potential temperature with a centered second-order advection scheme. Only the subset of panels that differ from those in Fig. C1 are shown, namely, the diapycnal advection, diapycnal shear, diapycnal Reynolds stresses, and thickness error.

consistently balancing the thickness and momentum budget. Instead, these studies construct the 3D TWA velocity, $\mathbf{v}^{\#}$, to be divergence-free: the horizontal TWA velocity is computed, its horizontal divergence calculated, and $w^{\#}$ obtained by vertical integration. This does not translate into buoyancy coordinates to give a diapycnal velocity ϖ as small as the model's buoyancy forcing. Cessi and Wolfe (2013) recognize a "striking cancellation" between the mean and eddy-induced diapycnal velocity in their model eastern boundary current. While this may be true, their residual diapycnal velocity may well be an order of magnitude larger than the actual diapycnal velocity ϖ. Nonetheless, Cessi and Wolfe (2013) develop a TWA PV budget, but only by ignoring the diapycnal velocity (among other terms), which could be far larger in their budgets than they believe, and not negligible. TWA manipulations of z-level model data that do not accurately balance the thickness equation should be regarded with skepticism.

REFERENCES

Aoki, K., A. Kubokawa, R. Furue, and H. Sasaki, 2016: Influence of eddy momentum fluxes on the mean flow of the Kuroshio extension in a 1/10° ocean general circulation model. *J. Phys. Oceanogr.*, **46**, 2769–2784, https://doi.org/10.1175/JPO-D-16-0021.1.

Arakawa, A., and V. R. Lamb, 1977: Computational design of the basic dynamical processes of the UCLA general circulation model. *Methods Comput. Phys.*, **17**, 173–265, https://doi.org/10.1016/B978-0-12-460817-7.50009-4.

Bodnariuk, N., C. G. Simionato, M. Saraceno, M. Osman, and L. B. Diaz, 2021: Interannual variability of the latitude of separation of the Brazil current: Teleconnections and oceanic Rossby waves propagation. *J. Geophys. Res. Oceans*, **126**, e2021JC017557, https://doi.org/10.1029/2021JC017557.

Cessi, P., and C. L. Wolfe, 2013: Adiabatic eastern boundary currents. *J. Phys. Oceanogr.*, **43**, 1127–1149, https://doi.org/10.1175/JPO-D-12-0211.1.

Combes, V., and R. P. Matano, 2014: Trends in the Brazil/Malvinas Confluence region. *Geophys. Res. Lett.*, **41**, 8971–8977, https://doi.org/10.1002/2014GL062523.

Danabasoglu, G., J. C. McWilliams, and P. R. Gent, 1994: The role of mesoscale tracer transports in the global ocean circulation. *Science*, **264**, 1123–1126, https://doi.org/10.1126/science.264.5162.1123.

Dellar, P. J., 2011: Variations on a beta-plane: Derivation of non-traditional beta-plane equations from Hamilton's principle on a sphere. *J. Fluid Mech.*, **674**, 174–195, https://doi.org/10.1017/S0022112010006464.

de Szoeke, R. A., 2000: Equations of motion using thermodynamic coordinates. *J. Phys. Oceanogr.*, **30**, 2814–2829, https://doi.org/10.1175/1520-0485(2001)031<2814:>2.0.CO;2.

——, S. R. Springer, and D. M. Oxilia, 2000: Orthobaric density: A thermodynamic variable for ocean circulation studies. *J. Phys. Oceanogr.*, **30**, 2830–2852, https://doi.org/10.1175/1520-0485(2001)031<2830:>2.0.CO;2.

Dewar, W. K., and A. M. Hogg, 2010: Topographic inviscid dissipation of balanced flow. *Ocean Modell.*, **32**, 1–13, https://doi.org/10.1016/j.ocemod.2009.03.007.

Gent, P. R., J. Willebrand, T. J. McDougall, and J. C. McWilliams, 1995: Parameterizing eddy-induced tracer transports in ocean circulation models. *J. Phys. Oceanogr.*, **25**, 463–474, https://doi.org/10.1175/1520-0485(1995)025<0463:PEITTI>2.0.CO;2.

Gille, S. T., 1997: Why potential vorticity is not conserved along mean streamlines in a numerical Southern Ocean. *J. Phys. Oceanogr.*, **27**, 1286–1299, https://doi.org/10.1175/1520-0485(1997)027<1286:WPVINC>2.0.CO;2.

Graham, R. M., and A. M. De Boer, 2013: The dynamical subtropical front. *J. Geophys. Res. Oceans*, **118**, 5676–5685, https://doi.org/10.1002/jgrc.20408.

Hughes, C. W., 1995: Rossby waves in the Southern Ocean: A comparison of TOPEX/POSEIDON altimetry with model predictions. *J. Geophys. Res.*, **100**, 15 933–15 950, https://doi.org/10.1029/95JC01380.

——, 1997: Comments on "On the obscurantist physics of 'form drag' in theorizing about the Circumpolar Current." *J. Phys. Oceanogr.*, **27**, 209–210, https://doi.org/10.1175/1520-0485(1997)027<0209:COOTOP>2.0.CO;2.

——, and B. A. De Cuevas, 2001: Why western boundary currents in realistic oceans are inviscid: A link between form stress and bottom pressure torques. *J. Phys. Oceanogr.*, **31**, 2871–2885, https://doi.org/10.1175/1520-0485(2001)031<2871:WWBCIR>2.0.CO;2.

——, M. S. Jones, and S. Carnochan, 1998: Use of transient features to identify eastward currents in the Southern Ocean. *J. Geophys. Res.*, **103**, 2929–2943, https://doi.org/10.1029/97JC02442.

Johnson, G. C., and H. L. Bryden, 1989: On the size of the Antarctic Circumpolar Current. *Deep-Sea Res.*, **36A**, 39–53, https://doi.org/10.1016/0198-0149(89)90017-4.

Jones, C. S., and P. Cessi, 2016: Interbasin transport of the meridional overturning circulation. *J. Phys. Oceanogr.*, **46**, 1157–1169, https://doi.org/10.1175/JPO-D-15-0197.1.

Killworth, P. D., 1992: An equivalent-barotropic mode in the fine resolution Antarctic model. *J. Phys. Oceanogr.*, **22**, 1379–1387, https://doi.org/10.1175/1520-0485(1992)022<1379:AEBMIT>2.0.CO;2.

Klocker, A., and D. P. Marshall, 2014: Advection of baroclinic eddies by depth mean flow. *Geophys. Res. Lett.*, **41**, 3517–3521, https://doi.org/10.1002/2014GL060001.

Lu, Y., and D. Stammer, 2004: Vorticity balance in coarse-resolution global ocean simulations. *J. Phys. Oceanogr.*, **34**, 605–622, https://doi.org/10.1175/2504.1.

Lumpkin, R., and S. Garzoli, 2011: Interannual to decadal changes in the western South Atlantic's surface circulation. *J. Geophys. Res.*, **116**, C01014, https://doi.org/10.1029/2010JC006285.

MacCready, P., and P. B. Rhines, 2001: Meridional transport across a zonal channel: Topographic localization. *J. Phys. Oceanogr.*, **31**, 1427–1439, https://doi.org/10.1175/1520-0485(2001)031<1427:MTAAZC>2.0.CO;2.

Marshall, D. P., 1995: Topographic steering of the Antarctic circumpolar current. *J. Phys. Oceanogr.*, **25**, 1636–1650, https://doi.org/10.1175/1520-0485(1995)025<1636:TSOTAC>2.0.CO;2.

——, 1997: Subduction of water masses in an eddying ocean. *J. Mar. Res.*, **55**, 201–222, https://doi.org/10.1357/0022240973224373.

——, D. R. Munday, L. C. Allison, R. J. Hay, and H. L. Johnson, 2016: Gill's model of the Antarctic Circumpolar Current, revisited: The role of latitudinal variations in wind stress. *Ocean Modell.*, **97**, 37–51, https://doi.org/10.1016/j.ocemod.2015.11.010.

Marshall, J., and T. Radko, 2003: Residual-mean solutions for the Antarctic Circumpolar Current and its associated overturning circulation. *J. Phys. Oceanogr.*, **33**, 2341–2354, https://doi.org/10.1175/1520-0485(2003)033<2341:RSFTAC>2.0.CO;2.

Masich, J., T. K. Chereskin, and M. R. Mazloff, 2015: Topographic form stress in the Southern Ocean state estimate. *J. Geophys. Res. Oceans*, **120**, 7919–7933, https://doi.org/10.1002/2015JC011143.

Matano, R. P., 1993: On the separation of the Brazil current from the coast. *J. Phys. Oceanogr.*, **23**, 79–90, https://doi.org/10.1175/1520-0485(1993)023<0079:OTSOTB>2.0.CO;2.

Mazloff, M. R., P. Heimbach, and C. Wunsch, 2010: An eddy-permitting Southern Ocean state estimate. *J. Phys. Oceanogr.*, **40**, 880–899, https://doi.org/10.1175/2009JPO4236.1.

McDougall, T. J., 1987: Neutral surfaces. *J. Phys. Oceanogr.*, **17**, 1950–1964, https://doi.org/10.1175/1520-0485(1987)017<1950:NS>2.0.CO;2.

——, 1989: Streamfunctions for the lateral velocity vector in a compressible ocean. *J. Mar. Res.*, **47**, 267–284, https://doi.org/10.1357/002224089785076271.

——, and D. R. Jackett, 1988: On the helical nature of neutral trajectories in the ocean. *Prog. Oceanogr.*, **20**, 153–183, https://doi.org/10.1016/0079-6611(88)90001-8.

——, and P. C. McIntosh, 1996: The temporal-residual-mean velocity. Part I: Derivation and the scalar conservation equations. *J. Phys. Oceanogr.*, **26**, 2653–2665, https://doi.org/10.1175/1520-0485(1996)026<2653:TTRMVP>2.0.CO;2.

——, and ——, 2001: The temporal-residual-mean velocity. Part II: Isopycnal interpretation and the tracer and momentum equations. *J. Phys. Oceanogr.*, **31**, 1222–1246, https://doi.org/10.1175/1520-0485(2001)031<1222:TTRMVP>2.0.CO;2.

Montgomery, R., 1937: A suggested method for representing gradient flow in isentropic surfaces. *Bull. Amer. Meteor. Soc.*, **18**, 210–212, https://doi.org/10.1175/1520-0477-18.6-7.210.

Munk, W. H., and E. Palmén, 1951: Note on the dynamics of the Antarctic Circumpolar Current. *Tellus*, **3**, 53–55, https://doi.org/10.3402/tellusa.v3i1.8609.

Olbers, D., 1998: Comments on "On the obscurantist physics of 'form drag' in theorizing about the Circumpolar Current." *J. Phys. Oceanogr.*, **28**, 1647–1654, https://doi.org/10.1175/1520-0485(1998)028<1647:COOTOP>2.0.CO;2.

Ridgway, K. R., and J. R. Dunn, 2007: Observational evidence for a Southern Hemisphere oceanic supergyre. *Geophys. Res. Lett.*, **34**, L13612, https://doi.org/10.1029/2007GL030392.

Smith, K. S., 2007: The geography of linear baroclinic instability in Earth's oceans. *J. Mar. Res.*, **65**, 655–683, https://doi.org/10.1357/002224007783649484.

Stanley, G. J., 2019a: Neutral surface topology. *Ocean Modell.*, **138**, 88–106, https://doi.org/10.1016/j.ocemod.2019.01.008.

——, 2019b: The exact geostrophic streamfunction for neutral surfaces. *Ocean Modell.*, **138**, 107–121, https://doi.org/10.1016/j.ocemod.2019.04.002.

——, T. E. Dowling, M. E. Bradley, and D. P. Marshall, 2020: Ertel potential vorticity versus Bernoulli potential on approximately neutral surfaces in the Antarctic Circumpolar Current. *J. Phys. Oceanogr.*, **50**, 2621–2648, https://doi.org/10.1175/JPO-D-19-0140.1.

Stewart, A. L., J. C. McWilliams, and A. Solodoch, 2021: On the role of bottom pressure torques in wind-driven gyres. *J. Phys. Oceanogr.*, **51**, 1441–1464, https://doi.org/10.1175/JPO-D-20-0147.1.

Stommel, H., 1957: A survey of ocean current theory. *Deep-Sea Res.*, **4**, 149–184, https://doi.org/10.1016/0146-6313(56)90048-X.

Sverdrup, H. U., 1947: Wind-driven currents in a baroclinic ocean; with application to the equatorial currents of the eastern Pacific. *Proc. Natl. Acad. Sci. USA*, **33**, 318–326, https://doi.org/10.1073/pnas.33.11.318.

Tamsitt, V., and Coauthors, 2017: Spiraling pathways of global deep waters to the surface of the Southern Ocean. *Nat. Commun.*, **8**, 172, https://doi.org/10.1038/s41467-017-00197-0.

Tansley, C. E., and D. P. Marshall, 2001: On the dynamics of wind-driven circumpolar currents. *J. Phys. Oceanogr.*, **31**, 3258–3273, https://doi.org/10.1175/1520-0485(2001)031<3258:OTDOWD>2.0.CO;2.

Thompson, A. F., A. L. Stewart, and T. Bischoff, 2016: A multibasin residual-mean model for the global overturning circulation. *J. Phys. Oceanogr.*, **46**, 2583–2604, https://doi.org/10.1175/JPO-D-15-0204.1.

Uchida, T., Q. Jamet, W. K. Dewar, D. Balwada, J. Lesommer, and T. Penduff, 2021: Diagnosing the thickness-weighted averaged eddy-mean flow interaction in an eddying North Atlantic ensemble, version 2. Earth and Space Science Open Archive, https://doi.org/10.1002/essoar.10504082.2.

Warren, B. A., J. H. LaCasce, and P. E. Robbins, 1996: On the obscurantist physics of "form drag" in theorizing about the Circumpolar Current. *J. Phys. Oceanogr.*, **26**, 2297–2301, https://doi.org/10.1175/1520-0485(1996)026<2297:OTOPOD>2.0.CO;2.

Young, W. R., 2010: Dynamic enthalpy, conservative temperature, and the seawater Boussinesq approximation. *J. Phys. Oceanogr.*, **40**, 394–400, https://doi.org/10.1175/2009JPO4294.1.

——, 2012: An exact thickness-weighted average formulation of the Boussinesq equations. *J. Phys. Oceanogr.*, **42**, 692–707, https://doi.org/10.1175/JPO-D-11-0102.1.

Zajaczkovski, U., 2017: A study of the Southern Ocean: Mean state, eddy genesis & demise, and energy pathways. Ph.D. thesis, University of California, San Diego, 125 pp.

Zhai, X., H. L. Johnson, and D. P. Marshall, 2010: Significant sink of ocean-eddy energy near western boundaries. *Nat. Geosci.*, **3**, 608–612, https://doi.org/10.1038/ngeo943.

Zhang, H.-M., and N. G. Hogg, 1992: Circulation and water mass balance in the Brazil Basin. *J. Mar. Res.*, **50**, 385–420, https://doi.org/10.1357/002224092784797629.